Photoexcitation and recombination processes of the neutral nitrogen-vacancy center in diamond from first principles

Gergő Thiering[1,*] and Adam Gali[1,2,3,†]

[1] *HUN-REN Wigner Research Centre for Physics, PO Box 49, H-1525, Budapest, Hungary*
[2] *Department of Atomic Physics, Institute of Physics, Budapest University of Technology and Economics, Műegyetem rakpart 3., H-1111 Budapest, Hungary*
[3] *MTA-WFK Lendület "Momentum" Semiconductor Nanostructures Research Group, PO Box 49, H-1525, Budapest, Hungary*

Nitrogen-vacancy (NV) complex in diamond is one of the most prominent solid state defects as the negatively charged NV defect (NV^-) is a leading contender for quantum technologies. In quantum information processing applications, NV^- is photoexcited that often leads to photoionization to neutral NV defect, NV^0, and re-ionization back to NV^- should occur to control the $S = 1$ spin of NV^-. As a consequence, understanding the photophysics of NV^0 is crucial for controlling NV^-. Furthermore, recent studies have shown that the $S = 1/2$ electron spin of NV^0 can be also initialized and read out at certain conditions that turns single NV^0 a potential quantum bit. Quantum optics protocols rest on detailed knowledge on the electronic structure of the given system which is obviously missing for NV^0 in diamond. In this study, we combine group theory and density functional theory calculations towards exploring the nature of the ground and excited states of NV^0. We show that the effective three-electron system of NV^0 leads to high correlation effects that makes this system very challenging for *ab initio* simulations.

I. INTRODUCTION

Nitrogen-vacancy (NV) center[1] in diamond has been received a continuous interest due to its broad applicability for quantum technologies[2–8]. Most of these applications utilize its negative charge state (NV^-) that belongs to the 637 nm[1] (1.945 eV) zero-phonon-line (ZPL) photoluminescence center. The NV^- color center possesses $S = 1$ electronic spin that can be initialized, coherently driven and read out, thus NV^- may act as an exemplary qubit operating at room temperature[9–12]. An early theoretical work suggested[13] that the neutral counterpart, NV^0, may also act as a qubit. This has been recently realized in experiments[14–17] where NV^0 possess $S = 1/2$ electronic spin in the ground state with the corresponding 575 nm (2.156 eV) ZPL emission (Fig. 1). However, in stark contrast to the extensively studied NV^-, various magneto-optical properties of NV^0 are vaguely studied and the underlying physics is left unknown.

Both 1.945 eV[2,18–20] and 2.156 eV[21,22] color centers are active in both absorption (ABS) and photoluminescence (PL) processes. NV^- defect's 1.945 eV ZPL is accompanied[19] by a broad phonon sideband both in PL and ABS exhibiting only minor asymmetry [c.f., Figs. 2(c) and (d)]. The sideband mainly couples to a $\hbar\omega = 64$ meV quasilocal vibration and the strength of coupling can be depicted by $S \approx 3.5$ Huang-Rhys (HR) factor. Consequently, the ZPL exhibits a Debye-Waller factor of $DW = e^{-S} \approx 3\%$ thus only 3% of total intensity resides in the ZPL in agreement with previous *ab initio* simulations within[23,24] and beyond the HR approach[25].

Both 1.945-eV and 2.156-eV ZPLs are attributed to transitions between the same a_1 and e electronic orbitals [Fig. 1(b)] that would imply comparable optical features. Surprisingly, however, there is a significant asymmetry in NV^0 defect's PL and ABS phonon sidebands as plotted

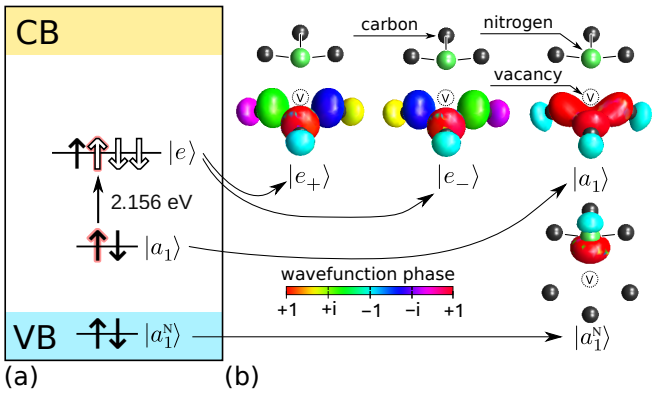

FIG. 1. Electronic structure of the neutral nitrogen-vacancy (NV^0) center of diamond. (a) Defect levels inside the band gap of diamond. (b) Single particle (Kohn-Sham) orbitals of defect levels.

in Figs. 2(a) and (b), respectively. $S = 2.35$ HR factor of the PL spectrum was reported for NV^0 defect[26] and another study reported $S = 1.9(1)$ at 77 K (Ref. 15). ABS spectra exhibits much broader sideband quantified by an $S = 3.9$ HR factor[21]. Interestingly, the PL signal is coupled to phonons with significantly smaller energy $\hbar\omega \approx$ 42-45 meV[15,27] than those of NV^-. The radiative lifetime of the excited state of NV^0 is reported as 13.2(2)[28], 19(2)[29], 17(1)[30], 20(1)[31] ns in different studies.

The 2.156-eV ZPL of NV^0 occurs between ^2E orbitally degenerate ground state to an orbitally non-degenerate $^2A_2$ confirmed by uniaxial stress measurements[21,34]. Furthermore, ^2E splits to two Kramers doublets ($E_{1/2}$ and $E_{3/2}$) due to spin-orbit coupling. In this context, we note that NV^- defect's spin-orbit splitting was already reported as $\lambda = 5.3$ GHz[35] or $\lambda = 5.33(3)$ GHz[36] by var-

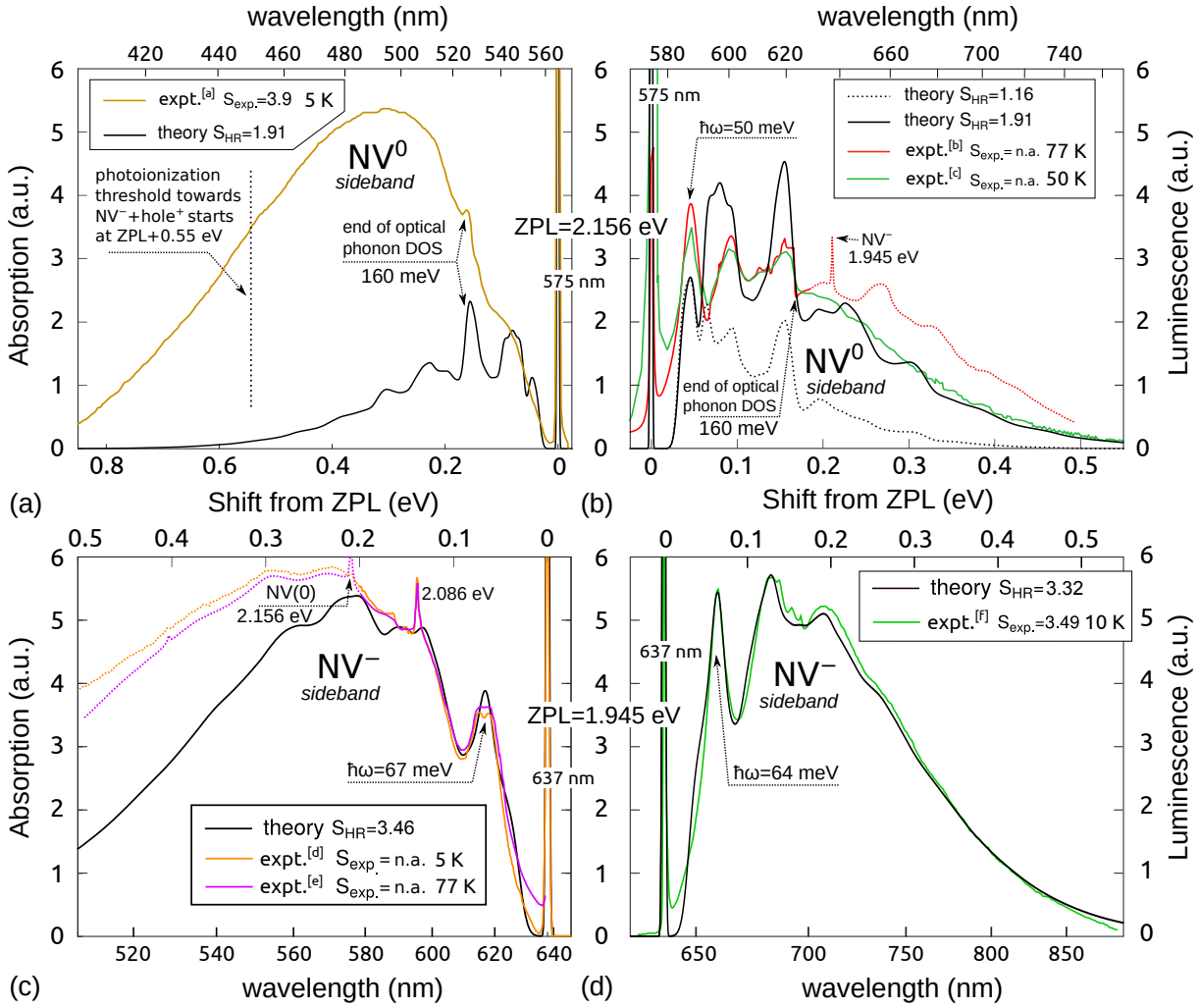

FIG. 2. Comparison of theoretical and experimental phonon sidebands for the negative and neutral NV defects. (a,c) Absorption lineshape of the 2.156-eV and 1.945-eV peaks of NV^0 and NV^-, respectively. We scaled the experimental and theoretical lineshapes to exhibit the same area under their curves between the ZPL and 100 meV, 200 meV for NV^0, NV^- respectively. (b,d) Luminescence lineshapes for 2.156-eV NV^0 and 1.945-eV NV^-, respectively. We normalized the experimental (expt.) and theoretical lineshapes in their full range. Expt. data are taken from different sources as follows: [a]: Fig. 1(b) from Ref. 21 [b]: Fig. 2(a) data from Ref. 29 at 1400°C anneal. [c]: Ref. 32 [d]: Fig. 4 in Ref. 33 [e]: Fig. 6(b) in Ref. 19 [f]: Fig. 3(b) in Ref. 20 .

ious experiments more than a decade ago, yet the λ for NV^0 has not been reported until recently. The exact spin-orbit splitting value[37] is still ambiguous as $\lambda = 4.48(10)$[14] and 9.8(8)[16] GHz were reported by two different research groups. Additionally, we note that electron paramagnetic resonance (EPR) for NV^0 defect's $S = 1/2$ spin has not yet been reported, to our best knowledge. The lack of EPR signal is attributed to linewidth broadening caused by the Jahn-Teller effect[38,39].

On the other hand, under continuous green illumination at 532 nm, an $S = 3/2$ spin associated with the metastable $^4A_2$ state of NV^0 was indeed observed in EPR[38] where early *ab initio* calculations confirmed the model based on the favorable comparison of the observed and calculated hyperfine signatures between the $S = 3/2$ electron spin and $I = 1/2$ ^{15}N ($A_\parallel = -35.7(3)$ MHz and $A_\perp = -23.8(3)$ MHz in experiments) and ^{13}C nuclear spins[13]. The observed near free electron g-factors ($g_\parallel = 2.0029(2)$, $g_\perp = 2.0035(2)$) imply very small second-order spin-orbit interaction associated with this state. In this case, the C_{3v} symmetric axial field causes a zero-field splitting between the $E_{1/2}$ and $E_{3/2}$ levels at $D = 1685(5)$ MHz as observed in the EPR spectrum[38].

The existence of the metastable $^4A_2$ state has been confirmed by *ab initio* calculations with various levels of theory[13,40–42]. However, the level position referenced to the ^2E ground state scatters between 0.4 eV to 0.86 eV (see Table I). According to a recent theoretical study with combining selection rules and ionization potentials of NV^- (Ref. 42), successive two-photon absorption of

NV^- via ^3E excited state could populate the $m_s = \pm 1/2$ state over the $m_s = \pm 3/2$ state of the $^4A_2$ state which would explain the occupation of the $^4A_2$ metastable state and the EPR signal of this metastable state under green optical pumping that is enhanced by the population difference in their spin levels. This theory sets the position the $^4A_2$ level over ^2E level at around 0.4 eV.

This example shows that it is crucial to know the lifetime of this metastable state so one can reliably setup quantum optics protocols for this potential qubit state. This is associated with the intersystem crossing (ISC) between $^4A_2$ and ^2E as well as the photoionization cross-section from $^4A_2$ to the ionization bands. To our knowledge, this issue has not yet been resolved for NV^0 as well as the origin on the phonon sidebands of the absorption and luminescence spectra. In this study, we aim to understand the photophysics of NV^0 and the non-radiative decay routes that are all associated with the strong electron-phonon coupling of the system.

The paper is organized as follows. In Sec. II we describe our *ab initio* methodology. Then, we depict the electronic structure of NV^0 and establish the nomenclature of our paper in Sec. III. Next, we discuss the interactions that governs the ^2E ground state and its optical excitation at 2.156-eV in Sec. IV. After understanding both spin-orbit and electron-phonon couplings of NV^0, we show and discuss our results on the ISC rates of $^4A_2$ in Sec. V and the photoionization threshold energies and processes in Sec. VI. Finally, we will conclude our paper in Sec. VII.

II. METHODOLOGY ON ATOMISTIC SIMULATIONS

We apply *ab initio* calculations with the use of simple cubic 512-atom supercells embedding NV defect within the framework of spinpolarized density functional theory (DFT) as implemented in the VASP 5.4.1 code[43]. The 512-atom model suffices to sample the Brillouin zone of the supercell at the Γ point. We converged the electronic structure by self-consistent cycles with 10^{-5} eV convergence threshold. The applied projector-augmentation-wave method (PAW)[44,45] on the core electron orbitals made possible to use a relatively low cutoff (370 eV) plane wave basis for electron wavefunctions. We converged the forces acting on ions below 10^{-3} eV/Å.

We applied the Heyd-Scuseria-Ernzerhof (HSE06) hybrid functional[46,47] that reproduces the experimental band gap and the charge transition levels of defects in Group-IV semiconductors within 0.1 eV accuracy[48,49]. We determined the excitation energies for excited states within 0.1 eV accuracy with the ΔSCF method[50] that provides accurate ZPL energy and Stokes-shift for the optical excitation spectra of the triplets of NV center[23,24] and group-IV impurity-vacancy centers[51,52] of diamond.

We used the HR theory[23,53,54] to predict the phonon sidebands near the ZPL emission. We used the Perdew-Burke-Ernzerhof (PBE) semilocal functional[55] to determine the vibration frequencies and eigenvectors as PBE is reported to accurately predict these features[23]. However, we employed the computationally demanding HSE06 to determine the optical excitation energies by means of the ΔSCF method where the atomic positions upon excitation are relaxed.

We determined the spin-orbit coupling as implemented in the VASP code within the scalar-relativistic approximation[56]. During the non-collinear calculations for spin-orbit coupling we fixed the spin quantization axis along the trigonal symmetry axis of the defect. We determined the spin-orbit coupling parameters directly from matrix elements between single particle Kohn-Sham orbitals that reproduced the observed fine structure of defects within 20% accuracy[24,51,52,57,58].

III. PRELIMINARIES: ELECTRONIC STRUCTURE

Here we define the basic nomenclature of the paper. We note that the orbitals and levels of NV^- from DFT calculations have been already published in several papers[40,59–66]. Furthermore, the respective many-body states and spin-orbit coupling coefficients acting between them were also thoroughly analyzed[67,68]. As we will show in this paper, the strong electron-phonon coupling should be explicitly considered for the many-body states of NV^0 that was lacking in previous studies. Therefore, instead of referring towards these papers, we explicitly reiterate the respective wavefunctions and interactions that we use in the entire paper. Therefore, we begin our discussion presenting electronic structure of NV^0 in Sec. III A. We describe the different forms of electronic correlations governing multiconfigurational character $|^2E\rangle$, $|^4A_2\rangle$, $|^2A_2\rangle$, $|^2E^*\rangle$ multiplets of NV^0 in Sections III B-III D. We summarize the multiplet energies within different levels of theory from the literature accompanied by our present results in Table I.

A. Electronic structure of NV^0

The NV defect introduces an a_1 and a double degenerate e level in the gap (see Fig. 1) that are occupied by three electrons in the relevant neutral charge state. The $|^2E'\rangle$ ground state has (aae) electron occupation. The $|^2E'\rangle$ multiplet is split into two $|^2E'_{\frac{1}{2}}\rangle$ and $|^2E'_{\frac{3}{2}}\rangle$ Kramer's doublets as

$$\begin{aligned} |^2E'_{+\frac{3}{2}}\rangle &= \mathcal{A}|a_1^{\uparrow}a_1^{\downarrow}e_+^{\uparrow}\rangle, & |^2E'_{+\frac{1}{2}}\rangle &= \mathcal{A}|a_1^{\downarrow}a_1^{\uparrow}e_+^{\downarrow}\rangle, \\ |^2E'_{-\frac{3}{2}}\rangle &= \mathcal{A}|a_1^{\downarrow}a_1^{\uparrow}e_-^{\downarrow}\rangle, & |^2E'_{-\frac{1}{2}}\rangle &= \mathcal{A}|a_1^{\uparrow}a_1^{\downarrow}e_-^{\uparrow}\rangle \end{aligned} \quad (1)$$

where we label them by their m_j=$\pm\frac{1}{2}, \pm\frac{3}{2}$ total angular momentum that includes both spin m_s=($\uparrow$,$\downarrow$) and effective orbital momentum (m_l=$\pm$1) from e levels by introducing $|e_\pm\rangle = \frac{1}{\sqrt{2}}(|e_x\rangle \pm i|e_y\rangle)$ complex combination of

TABLE I. Electronic excited states for NV^0. All energies are in eV units. We note that we optimized the atomic positions of atoms in our present work (p.w.) with HSE06, PBE, LDA functionals. However, the atomic positions were not relaxed within configuration interaction (conf. int.)[c] and Hubbard modeling (Hubbard)[d] results.

method	$\|^4A_2\rangle$	$\|^2A_2\rangle$	$\|^2E^*\rangle$	$\|^2A_1\rangle$
expt.	$\sim$0.4[a]	2.156	n.a.	n.a.
HSE06	$0.48^{\text{p.w.}}$	$2.36^{\text{p.w.}}$	$2.33^{\text{p.w.}}$	$\sim 2.8^{\text{p.w.}}$
PBE	$0.58^{\text{p.w.}}$	$1.20^{\text{p.w.}}$	$1.24^{\text{p.w.}}$	n.a
LDA	0.86[b]	$1.22^{\text{p.w.}}$	$1.26^{\text{p.w.}}$	n.a
conf. int.	0.68[c]	1.65[c]	2.04[c]	2.93[c]
Hubbard	0.68[d]	2.64[d]	2.88[d]	3.29[d]

[a] Although directly not known, the difference between photoionization thresholds of $|^3A_2\rangle \to |^2E\rangle$ and $|^3E\rangle \to |^4A_2\rangle$ are 432 meV and 342 meV, respectively, which hints for $\sim$0.415 eV energy position for the $|^4A_2\rangle$ multiplet. However, these photoionization thresholds were recorded at room temperature where phonon-assisted transition can also occur thus $\sim$0.415 eV is still an estimate.
[b] *Ab-initio* taken data from Ref. 13
[c] *Ab-initio* data by means of screened configuration interaction on top of LDA (*local density approximation* of DFT) from Ref. 41
[d] *Ab-initio* data by means of generalized Hubbard Hamiltonian on top of B3LYP functional from Ref. 40 in a $C_{71}H_{85}$ diamond molecular cluster

the $e_{\{x,y\}}$ real orbitals. Electronic excitation of NV^0 will promote an electron from the $|a_1\rangle$ orbital to an $|e\rangle$ orbital giving rise the (aee) electronic configuration. We construct these states as tensor products of NV^- with (ee) configurations coupled to an (a) hole. The latter can be labeled as $|^2A_1\rangle$ while the (ee) gives rise the following $|^3A_2\rangle \oplus |^1E\rangle \oplus |^1A_1\rangle$ two particle wave-functions,

$$\begin{aligned}
|^3A_2^+\rangle &= \mathcal{A}|e_+^\uparrow e_-^\uparrow\rangle,\\
|^3A_2^0\rangle &= \tfrac{1}{\sqrt{2}}\big(\mathcal{A}|e_+^\uparrow e_-^\downarrow\rangle + \mathcal{A}|e_+^\downarrow e_-^\uparrow\rangle\big),\\
|^3A_2^-\rangle &= \mathcal{A}|e_+^\downarrow e_-^\downarrow\rangle,\\
|^1E_\pm\rangle &= \mathcal{A}|e_\pm^\uparrow e_\mp^\downarrow\rangle,\\
|^1A_1\rangle &= \tfrac{1}{\sqrt{2}}\big(\mathcal{A}|e_+^\uparrow e_-^\downarrow\rangle - \mathcal{A}|e_-^\downarrow e_+^\uparrow\rangle\big).
\end{aligned} \tag{2}$$

We then take the combinations with the additional $|a_1\rangle$ orbital thus the optically excited states can be labeled as

$$\Big[|^3A_2\rangle \oplus |^1E\rangle \oplus |^1A_1\rangle\Big] \otimes \Big[|^2A_1\rangle\Big] = |^4A_2\rangle \oplus |^2A_2\rangle \oplus |^2E\rangle \oplus |^2A_1\rangle. \tag{3}$$

According to Hund's first rule, $|^4A_2\rangle$ with maximized spin is the lowermost excited state

$$\begin{aligned}
|^4A_2^{+\frac{3}{2}}\rangle &= \mathcal{A}|a_1^\uparrow e_-^\uparrow e_+^\uparrow\rangle,\\
|^4A_2^{+\frac{1}{2}}\rangle &= \tfrac{1}{\sqrt{3}}\big(\mathcal{A}|a_1^\uparrow e_-^\uparrow e_+^\downarrow\rangle + \mathcal{A}|a_1^\uparrow e_-^\downarrow e_+^\uparrow\rangle + \mathcal{A}|a_1^\downarrow e_-^\uparrow e_+^\uparrow\rangle\big),\\
|^4A_2^{-\frac{1}{2}}\rangle &= \tfrac{1}{\sqrt{3}}\big(\mathcal{A}|a_1^\downarrow e_+^\uparrow e_-^\downarrow\rangle + \mathcal{A}|a_1^\downarrow e_+^\downarrow e_-^\uparrow\rangle + \mathcal{A}|a_1^\uparrow e_+^\downarrow e_-^\downarrow\rangle\big),\\
|^4A_2^{-\frac{3}{2}}\rangle &= \mathcal{A}|a_1^\downarrow e_+^\downarrow e_-^\downarrow\rangle.
\end{aligned} \tag{4}$$

The triplet configuration $|^3A_2\rangle$ may couple to $|^2A_1\rangle$ with opposite spins that results in

$$\begin{aligned}
|^2A_2^+\rangle &= \tfrac{1}{\sqrt{6}}\big(\mathcal{A}|a_1^\uparrow e_-^\uparrow e_+^\downarrow\rangle + \mathcal{A}|a_1^\uparrow e_-^\downarrow e_+^\uparrow\rangle - 2\mathcal{A}|a_1^\downarrow e_-^\uparrow e_+^\uparrow\rangle\big),\\
|^2A_2^-\rangle &= \tfrac{1}{\sqrt{6}}\big(\mathcal{A}|a_1^\downarrow e_+^\downarrow e_-^\uparrow\rangle + \mathcal{A}|a_1^\downarrow e_+^\uparrow e_-^\downarrow\rangle - 2\mathcal{A}|a_1^\uparrow e_+^\downarrow e_-^\downarrow\rangle\big)
\end{aligned} \tag{5}$$

multiplets. Additionally, $|^1E\rangle$ singlet can couple to $|a_1\rangle$ that gives rise

$$\begin{aligned}
|^2E''_{+\frac{3}{2}}\rangle &= \mathcal{A}|a_1^\uparrow e_-^\downarrow e_-^\uparrow\rangle, & |^2E''_{+\frac{1}{2}}\rangle &= \mathcal{A}|a_1^\downarrow e_-^\uparrow e_-^\downarrow\rangle,\\
|^2E''_{-\frac{3}{2}}\rangle &= \mathcal{A}|a_1^\downarrow e_+^\uparrow e_+^\downarrow\rangle, & |^2E''_{-\frac{1}{2}}\rangle &= \mathcal{A}|a_1^\uparrow e_+^\downarrow e_+^\uparrow\rangle.
\end{aligned} \tag{6}$$

When $|^1A_1\rangle$ couples to $|^2a_1\rangle$ then it results in $|^2A_1\rangle$ that can be written as

$$\begin{aligned}
|^2A_1^+\rangle &= \tfrac{1}{\sqrt{2}}\big(\mathcal{A}|a_1^\uparrow e_-^\uparrow e_+^\downarrow\rangle - \mathcal{A}|a_1^\uparrow e_-^\downarrow e_+^\uparrow\rangle\big),\\
|^2A_1^-\rangle &= \tfrac{1}{\sqrt{2}}\big(\mathcal{A}|a_1^\downarrow e_+^\downarrow e_-^\uparrow\rangle - \mathcal{A}|a_1^\downarrow e_+^\uparrow e_-^\downarrow\rangle\big).
\end{aligned} \tag{7}$$

Finally, we show the high-energy $|^2E'''\rangle$ state for the sake of completeness when all three electrons occupy the e levels as (eee) electronic configuration,

$$\begin{aligned}
|^2E'''_{+\frac{3}{2}}\rangle &= \mathcal{A}|e_-^\uparrow e_+^\downarrow e_+^\uparrow\rangle, & |^2E'''_{+\frac{1}{2}}\rangle &= \mathcal{A}|e_-^\downarrow e_+^\uparrow e_+^\downarrow\rangle,\\
|^2E'''_{-\frac{3}{2}}\rangle &= \mathcal{A}|e_+^\downarrow e_-^\uparrow e_-^\downarrow\rangle, & |^2E'''_{-\frac{1}{2}}\rangle &= \mathcal{A}|e_+^\uparrow e_-^\downarrow e_-^\uparrow\rangle.
\end{aligned} \tag{8}$$

However, these configurations can be excluded from the discussion as the corresponding levels lie higher than the ionization bands.

B. Dynamic correlation in the $|^2E\rangle$ ground state

We recognize in our spinpolarized DFT calculations that the symmetry of $|^2E\rangle$ is spontaneously broken even if the geometry is constrained to C_{3v} symmetry. That is, the orbitals follow the reduced C_{1h} symmetry where only a single $\hat{\sigma}$ mirror plane remains. Therefore, $|a_1\rangle$ level is allowed to mix with $|e_x\rangle$ because they both belong to A' representation while $|e_y\rangle$ cannot mix because it transform as the antisymmetric A'' representation. In order to identify electronic correlation in $|^2E\rangle$ we decompose the broken symmetry single determinant obtained by DFT into symmetric orbitals respecting C_{3v} symmetry as follows

$$\begin{aligned}
&\mathcal{A}|ua_1^\uparrow + ve_x^\uparrow; wa_1^\downarrow + le_x^\downarrow; e_y^\uparrow\rangle =\\
&\mathcal{A}\big(uw\underbrace{|a_1^\uparrow a_1^\downarrow e_y^\uparrow\rangle}_{=|^2E'\rangle\ \sim 71\,\%} + vw\underbrace{|e_x^\uparrow a_1^\downarrow e_y^\uparrow\rangle}_{\sim|^2A_2\rangle\ \sim 0.2\,\%} + ul\underbrace{|a_1^\uparrow e_x^\downarrow e_y^\uparrow\rangle}_{\sim|^2E''\rangle\ \sim 28\,\%} + vl\underbrace{|e_x^\uparrow e_x^\downarrow e_y^\uparrow\rangle}_{=|^2E'''\rangle\ \sim 0.1\,\%}
\end{aligned} \tag{9}$$

where $u = +0.998$, $v = -0.06$, $w = +0.85$, $l = -0.53$, thus $(uw)^2 = 0.71$, $(vw)^2 = 0.002$, $(ul)^2 = 0.28$, $(vl)^2 = 0.001$. Our results indicate that there is correlation in $|^2E'\rangle$. We note that the non-negligible $|^2A_2\rangle$ contribution occurs in the broken-symmetry solution as an artifact.

This term should be exactly zero with a multiconfigurational wavefunction method. Finally, the $|^2E'''\rangle$ contribution is only perturbative and can be again neglected. We additionally note that the $|a_1^{\uparrow}e_x^{\downarrow}e_y^{\uparrow}\rangle$ configuration is not a pure $|^2E''\rangle$ (see Sec. III D). However, we neglect this issue for the sake of simplicity and assume that all $|a_1^{\uparrow}e_x^{\downarrow}e_y^{\uparrow}\rangle$ electronic character belongs to $|^2E''\rangle$. To sum up, we assume that the two orbital doublet multiplets are mixed by the expressions,

$$\begin{aligned} |^2E_\Gamma\rangle &= c|^2E'_\Gamma\rangle + d|^2E''_\Gamma\rangle, \\ |^2E^*_\Gamma\rangle &= d|^2E'_\Gamma\rangle - c|^2E''_\Gamma\rangle, \end{aligned} \tag{10}$$

where Γ runs over $\Gamma = \{\pm\frac{1}{2}, \pm\frac{3}{2}\}$ and we used the $c^2 \approx (uw)^2$=71% (85%), $d^2 \approx (ul)^2$=28% (13%) parameters inherited from Eq. (9). We derived these parameters purely from DFT by means of HSE06 (PBE) functional. For comparison multiconfigurational methods report these parameters as $c^2 = 90\,\%$ and $d^2 = 8\,\%$ (see Table II. in the Supplemental Materials of Ref. 41).

We quantify the effect of electronic correlation in energy units by removing the symmetry constraint on the wavefunctions and enforcing C_{3v} symmetry only on the atomic positions. We report 12.5, 139, 891 meV energy gain by means of LDA, PBE, HSE06 functionals, respectively, where we enforce symmetrization by putting two electron halves on $|e_x\rangle$, $|e_y\rangle$ orbitals resulting in the $(a_{1\uparrow}^1 a_{1\downarrow}^1 e_{x\uparrow}^{0.5} e_{y\uparrow}^{0.5} e_{x\downarrow}^0 e_{y\downarrow}^0)$ electron occupation. We note that we determined the vibration frequencies and modes within this smeared occupation by means of PBE functional to avoid broken symmetry wavefunctions as given in Eq. (9). However, this introduces an artificial self-interaction as the electrons on $e_{x\downarrow}$ and $e_{y\downarrow}$ repel each other due to exchange integrals present in hybrid functionals such as HSE06. In summary, we highlight that the electronic correlation between the two $|^2E\rangle$, $|^2E^*\rangle$ multiplets is a significant effect that cannot be neglected. We set the reference point of our electronic total energy (for example in Fig. 3) to this broken symmetry solution on which we removed all possible symmetry constraints both on electronic and ionic degrees of freedom with the spinpolarized DFT method.

C. Correction scheme for $|^2A_2\rangle$ excited state

The single configuration that resembles $|^2A_2\rangle$ at largest extent that of Eq. (5) is the

$$\mathcal{A}|a_1^{\downarrow}e_-^{\uparrow}e_+^{\uparrow}\rangle = \sqrt{\frac{1}{3}}|^4A_2^{+\frac{1}{2}}\rangle - \sqrt{\frac{2}{3}}|^2A_2^{+}\rangle \tag{11}$$

determinant. In simple words, according to Eq. (11) the $\mathcal{A}|a_1^{\downarrow}e_-^{\uparrow}e_+^{\uparrow}\rangle$ configuration accessible within our DFT method corresponds to 66% of $|^2A_2\rangle$ and 33% of $|^4A_2\rangle$ character, respectively. In order to approximate the energy of multiconfigurational $|^2A_2\rangle$ we utilize a correction scheme similar to the method of von Barth originally proposed in 1979 (see Ref. 69). We multiply Eq. 11 in the left side by $\langle a_1^{\downarrow}e_-^{\uparrow}e_+^{\uparrow}|\mathcal{A}^\dagger\hat{H}_e$ that results in $E_{\mathrm{DFT}}\big(\mathcal{A}|a_1^{\downarrow}e_-^{\uparrow}e_+^{\uparrow}\rangle\big) = \langle a_1^{\downarrow}e_-^{\uparrow}e_+^{\uparrow}|\mathcal{A}^\dagger\hat{H}_e\mathcal{A}|a_1^{\downarrow}e_-^{\uparrow}e_+^{\uparrow}\rangle = \Big(\sqrt{\frac{1}{3}}\langle^4A_2^{+\frac{1}{2}}| - \sqrt{\frac{2}{3}}\langle^2A_2^{+}|\Big)\hat{H}_e\Big(\sqrt{\frac{1}{3}}|^4A_2^{+\frac{1}{2}}\rangle - \sqrt{\frac{2}{3}}|^2A_2^{+}\rangle\Big) = \frac{1}{3}E_{\mathrm{DFT}}\big(|^4A_2\rangle\big) + \frac{2}{3}E\big(|^2A_2\rangle\big)$ where $\hat{H}_e$ is the full electronic Hamiltonian and off-diagonal matrix elements $\langle^2A_2|\hat{H}_e|^4A_2\rangle$ are zeroes. Therefore, we can approximate the energy of multiconfigurational $|^2A_2\rangle$ excited state by the following scheme

$$E\big(|^2A_2\rangle\big) \approx \frac{3}{2}E_{\mathrm{DFT}}\big(\mathcal{A}|a_1^{\downarrow}e_-^{\uparrow}e_+^{\uparrow}\rangle\big) - \frac{1}{2}E_{\mathrm{DFT}}\big(|^4A_2\rangle\big), \tag{12}$$

where $E_{\mathrm{DFT}}\big(\mathcal{A}|a_1^{\downarrow}e_+^{\uparrow}e_-^{\uparrow}\rangle\big)$ = 1.22, 1.20, 1.74 eV with LDA, PBE, HSE06 functionals, respectively, and we allowed the atomic positions to relax and $E_{\mathrm{DFT}}\big(|^4A_2\rangle\big) = 0.86, 0.58, 0.48$ eV that of Table I. We note that this is only a crude approximation; nevertheless, we successfully applied this assumption in Eq. (6) of Ref. 70 and in Eq. (A5) in Ref. 52. In this case, we approximate the $|^2A_2\rangle$ level at 2.36 eV by means of HSE06 which experiences a correction on its Stokes-shift[49] by $\Delta E_{\mathrm{stokes}} = \hbar\omega\big[S\big(|^2A_2\rangle\big) - S\big(\mathcal{A}|a_1^{\downarrow}e_-^{\uparrow}e_+^{\uparrow}\rangle\big)\big]$ = 0.07 eV, where $S\big(|^2A_2\rangle\big)$ = 1.91, $S\big(\mathcal{A}|a_1^{\downarrow}e_-^{\uparrow}e_+^{\uparrow}\rangle\big)\big]$ = 1.16 and $\hbar\omega$ = 93.9 meV that yields 2.22 eV ZPL energy close to the experimentally observed data at 2.156 eV.

D. Correction scheme for $|^2E_2^*\rangle$ excited state

Similarly to considerations that of Sec. III C for $|^2A_2\rangle$ we estimate the energy of $|^2E^*\rangle$ excited state by left multiplying $\mathcal{A}|a_1^{\uparrow}e_x^{\downarrow}e_y^{\uparrow}\rangle = \sqrt{\frac{1}{2}}|E_{\frac{3}{2}}^{+}\rangle + \sqrt{\frac{1}{3}}|^4A_2^{+}\rangle + \sqrt{\frac{1}{6}}|^2A_2^{+}\rangle$ by $\langle a_1^{\uparrow}e_x^{\downarrow}e_y^{\uparrow}|\mathcal{A}^\dagger\hat{H}_e$. Therefore, the approximated energy of $|^2E^*\rangle$ will be

$$E\big(|^2E^*\rangle\big) \approx 2E_{\mathrm{DFT}}\big(|a_1^{\uparrow}e_x^{\downarrow}e_y^{\uparrow}\rangle\big) - \frac{2}{3}E\big(|^4A_2\rangle\big) - \frac{1}{3}E\big(|^2A_2\rangle\big), \tag{13}$$

where $E_{\mathrm{DFT}}\big(|a_1^{\uparrow}e_x^{\downarrow}e_y^{\uparrow}\rangle\big)$ = 1.26, 1.24, 1.72 eV for LDA, PBE, HSE06 functionals, respectively, where we allowed atomic positions to relax. We used Eq. (13) to determine excitation energies for Table I.

IV. NATURE OF THE GROUND STATE

Upon depicting the electronic structure of the $|^2E\rangle$ ground state, we aim to describe the observed fine structure of the $|^2E\rangle \leftrightarrow |^2A_2\rangle$ optical transition. We analyze the adjoint Jahn-Teller (Sec. IV A) and spin-orbit coupling (SOC) (Sec. IV B) effects. Additionally, local and external strain around the defect may affect the optical lines. Therefore, we will discuss both effects to approximate the λ effective SOC parameter that splits the $|^2E\rangle$ multiplet into two electron-phonon coupled doublets: $|\widetilde{E}_{\frac{1}{2}}\rangle$, $|\widetilde{E}_{\frac{3}{2}}\rangle$. Finally, we will discuss the possible excitation schemes from the ground state in Sec. IV D.

TABLE II. Jahn-Teller (JT) coupling parameters for the $|^2E\rangle$ ground state by means of various DFT functionals: LDA, PBE, HSE06.

	LDA[73]	LDA$^{\text{p.w.}}$	PBE$^{\text{p.w.}}$	HSE06$^{\text{p.w.}}$	expt.	
$\hbar\omega_E$:	62.5	64.5	63.5	62.5		meV
E_{JT}:	73.2	61.2	49.9	30.1		meV
δ_{JT}:	10	9.9	6.0	20.7		meV
$3\Gamma_{\text{tun.}}$[a]:	21.4	25.5	29.2	14.0	13.6[b]	meV
p factor:	0.118[c]	0.161	0.199	0.304		

[a] Energy of first vibronic excited state of JT system depicted by Eq. (14) known as tunneling splitting[71,72].

[b] Experimentally observed via uniaxial stress measurements[21] on the ZPL where 110 cm^{-1} fine structure was reported. Baier *et. al* reported this splitting as 12(2) and 13(4) meV by fitting thermal activation energy for an Orbach process[16].

[c] We applied Eq. (14) on data found in Ref. 73 to calculate the Ham reduction factor as expressed in Eq. (17).

A. Jahn-Teller effect in the $|^2E\rangle$ ground state

The ground state of NV^0 is a Jahn-Teller (JT) system where the $|^2E\rangle$ degenerate orbital interacts with a degenerate E vibration mode as the double degenerate e orbital is occupied by a single electron. We map the adiabatic potential energy by means of HSE06 functional to derive the JT Hamiltonian as

$$\hat{H}_{\text{DJT}} = \hbar\omega_E(a_X^\dagger a_X + a_Y^\dagger a_Y + 1) + F\big(\hat{X}\hat{\sigma}_z - \hat{Y}\hat{\sigma}_x\big) + G\big((\hat{X}^2 - \hat{Y}^2)\hat{\sigma}_z + 2\hat{X}\hat{Y}\hat{\sigma}_x\big) \quad (14)$$

acting between orbital $\hat{\sigma}_z = |^2E_x\rangle\langle^2E_x| - |^2E_y\rangle\langle^2E_y| = \left(\begin{smallmatrix}1 & \\ & -1\end{smallmatrix}\right)$, $\hat{\sigma}_x = |^2E_x\rangle\langle^2E_y| + |^2E_y\rangle\langle^2E_x| = \left(\begin{smallmatrix} & 1\\ 1 & \end{smallmatrix}\right)$ and vibrational $\hat{X} = (a_X^\dagger + a_X)/\sqrt{2}$, $\hat{Y} = (a_Y^\dagger + a_Y)/\sqrt{2}$ degrees of freedom. We determined the $\hbar\omega_E$ frequency of the harmonic oscillator by a parabola fit in the adiabatic potential energy surface (APES). We formulated F and G electron-phonon interaction strengths[71,72] from JT distortion energy as $E_{JT} = \{F^2/[2(\hbar\omega_E - 2G)]\}$ and the barrier energy as $\delta_{\text{JT}} = [(4E_{\text{JT}}G)/(\hbar\omega_E + 2G)]$. The computed first vibronic level (14.0 meV) is in excellent agreement with the experimentally observed one[21] at 13.6 meV (see Table II). Therefore we expect that our reported p Ham factor is reliable[24,71,72] that is used throughout our study.

B. Spin-orbit coupling in $|^2E\rangle$ ground state

Spin-orbit coupling (SOC) arises due to parallel or antiparallel spin and orbital momenta within $|e_{\mp}^{\uparrow,\downarrow}\rangle$ orbitals. Therefore the single particle spin-orbit operator can be depicted as

$$\hat{H}_{\text{SOC}} = \lambda_0\hat{l}_z\hat{s}_z + \lambda_\perp(\hat{l}_+\hat{s}_- + \hat{l}_-\hat{s}_+)/2, \quad (15)$$

where we show both parallel ($\hat{l}_z|e_\pm\rangle = \pm|e_\pm\rangle$) and perpendicular SOC components that flip the orbital character as $\hat{l}_\pm|a_1\rangle = \mp\sqrt{2}|e_\pm\rangle$[74]. We depict the electron spin

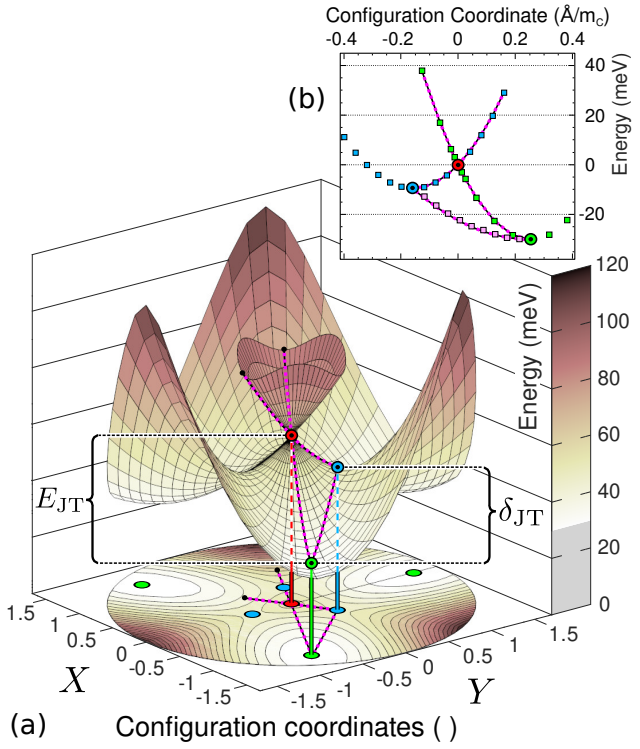

FIG. 3. Jahn-Teller effect for the ground state of NV^0. (a) Adiabatic potential energy surface (APES) of NV^0 defect's $|^2E\rangle$ ground state. We relaxed the atomic positions that of Jahn-Teller minima (green dots) and barrier saddle points (blue dots) C_{1h} by means of HSE06 functional. Additionally, we obtained the C_{3v} case (red dot) by enforcing symmetry constraints only on atomic positions and thus electronic correlation effects that of Eq. (9) can appear. Finally, we interpolated the geometries and calculated the electronic structure along the purple line to ensure the continuous shape of the APES. Additionally, we depict purple route in (b) inset that shows the raw HSE06 data points while (a) depicts the APES defined by Eq. (9) thus X and Y are dimensionless therein. We note that only the green and blue data points that of (a) follow the axis on the top while the purple data points do not.

by $\hat{s}_x = \frac{1}{2}\left(\begin{smallmatrix} & 1\\ 1 & \end{smallmatrix}\right)$, $\hat{s}_y = \frac{1}{2}\left(\begin{smallmatrix} & -i\\ i & \end{smallmatrix}\right)$, $\hat{s}_z = \frac{1}{2}\left(\begin{smallmatrix}1 & \\ & -1\end{smallmatrix}\right)$, $\hat{s}_\pm = \hat{s}_x \pm i\hat{s}_y$ standard spin operators.

One may recognize that the net effect of two e orbitals are completely canceled out for $|E''_{\frac{1}{2}/\frac{3}{2}}\rangle$ configurations (Eq. (6)) thus it is unaffected by any spin-orbit coupling. Therefore, only the $|E'_{\frac{1}{2}/\frac{3}{2}}\rangle$ configurations of Eq. (1) are subject splitting by λ_0 as

$$E\big(|E'_{\frac{1}{2}}\rangle\big) - E\big(|E'_{\frac{3}{2}}\rangle\big) = \langle e_+^\uparrow|\lambda_0\hat{l}_z\hat{s}_z|e_+^\uparrow\rangle - \langle e_-^\uparrow|\lambda_0\hat{l}_z\hat{s}_z|e_-^\uparrow\rangle. \quad (16)$$

Therefore, the spin-orbit coupling for the correlated $|E_{\frac{1}{2}/\frac{3}{2}}\rangle$ SOC parameter will be partially quenched by the c^2 correlation parameter of Eq. (10) and p Ham reduction factor[24,71,72] simultaneously as

$$\lambda_{\text{theory}} = p\lambda_z = pc^2\lambda_0, \quad (17)$$

where c^2 is the probability that the system is in the $|^2E'\rangle$

configuration and p is the Ham reduction factor of JT effect.

Firstly, we determined the λ_0 SOC parameter by constraining a half-half electron into $|e_{\pm}^{\uparrow}\rangle$ Kohn-Sham orbitals and leave $|e_{\pm}^{\downarrow}\rangle$ orbitals empty. This way, we completely cancel out the symmetry breaking effect both JT and electronic correlation origins thus the wavefunctions will be complex valued, that is, $|e_{\pm}\rangle$, where only spin-orbit coupling can split the degeneracy. We approximated the spin-orbit coupling parameters as $\lambda_0 = 290$ (318) GHz with HSE06 (PBE) functional depicting negligible difference on the choice of DFT functional.

We evaluate Eq. (16) by means of HSE06 functional, thus we used $c^2 = 0.71$, $p = 0.304$ and $\lambda_0 = 290$ GHz that results in $\lambda_{\text{theory}} = 31.4$ GHz that is significantly larger than that of the experimentally derived ones at $\lambda_{\text{expt.}} = 4.48$ GHz (Ref. 14) or 9.8 GHz (Ref. 16). The p and c^2 factors cannot correspond to this degree of discrepancy. Therefore we conclude that the $(a_{1\uparrow}^1 a_{1\downarrow}^1 e_{+\uparrow}^{0.5} e_{-\uparrow}^{0.5} e_{+\downarrow}^0 e_{-\downarrow}^0)$ constrained occupation that we forced upon our SOC calculations is not a reliable method. However, the broken symmetry solution of Eq. (9) cannot be used to this end as a and e orbitals are mixed in that case which also brings $\lambda_{\perp} \hat{l}_{\pm} \hat{s}_{\mp}$ matrix elements.

Nevertheless, we attempted to determine λ_0 from the correlated Eq. (9) wavefunction. Therefore, we determine λ_0 from the SOC matrix elements $|\langle u a_1^{\uparrow} + v e_x^{\uparrow} | \hat{H}_{SOC} | e_y^{\uparrow} \rangle| = v\lambda_0 \approx \lambda_0 = 71.1(74.7)$ GHz between unoccupied and occupied orbitals by means of HSE06 (PBE) functionals. However, it still overestimates experimental data as the reduced value is $pc^2\lambda_0 = 15.4$ GHz with HSE06 functional. We note that the λ_0 value might be estimated by the non-correlated e orbital in the ^3E excited state of NV^- which results in $\lambda_0 = 31.6$ GHz with HSE06 functional (Ref. 24). From this estimation the final spin-orbit gap yields $pc^2\lambda_0 = 6.8$ GHz. In summary, our results cannot accurately determine the spin-orbit gap from Kohn-Sham DFT level of theory because of the highly correlated nature of the $|^2E\rangle$ ground state.

Lastly, we note that we determine $\lambda_{\perp}$ as $\langle a_{1\downarrow} | \hat{H}_{\text{SOC}} | e_{-\uparrow} \rangle = \sqrt{2}\lambda_{\perp} = \sqrt{2} \times 107.3$ GHz matrix element as calculated from the $(a_{1\uparrow}^1 a_{1\downarrow}^1 e_{+\uparrow}^{0.5} e_{-\uparrow}^{0.5} e_{+\downarrow}^0 e_{-\downarrow}^0)$ constrained occupation. We use this $\lambda_{\perp}$ value for the ISC transition $|^2A_2\rangle \rightarrow |^2E\rangle$ (see Section V for details).

C. Quadrupolar and hyperfine parameters

We determine the hyperfine and quadrupolar parameters to a central ^{14}N nucleus as we described in Ref. 75. We used an increased (600 eV) plane wave basis for electron wavefunctions during the determination of spin parameters with HSE06 functional. The spin Hamiltonian that depicts the motion of ^{14}N nuclear spin ($I = 1$) goes as

TABLE III. Theoretical hyperfine and quadrupolar parameters for ^{14}N within $|^2E\rangle$ ground state.

$A_{\parallel} =$	-2.8	MHz	$A_{\perp} =$	-3.2	MHz
$A_1 =$	0.1	MHz	$A_2 =$	-0.1	MHz
$Q =$	-4.8	MHz			
$Q_1 =$	9.6	kHz	$Q_2 =$	-9.7	kHz

$$
\begin{aligned}
\hat{W}_{^{14}\text{N}} =& A_{\parallel} \hat{S}_z \hat{I}_z + A_{\perp} \left(\hat{S}_x \hat{I}_x + \hat{S}_y \hat{I}_y \right) + \\
& A_1 \left[(\hat{I}_x \hat{S}_z + \hat{I}_z \hat{S}_x)\hat{\sigma}_z + (\hat{I}_y \hat{S}_z + \hat{I}_y \hat{S}_x)\hat{\sigma}_x \right] + \\
& A_2 \left[(\hat{I}_y \hat{S}_y - \hat{I}_x \hat{S}_x)\hat{\sigma}_z + (\hat{I}_x \hat{S}_y + \hat{I}_y \hat{S}_x)\hat{\sigma}_x \right] + \\
& Q \left(\hat{I}_z^2 - \frac{1}{3} I(I+1) \right) + \\
& Q_1 \left[(\hat{I}_x \hat{I}_z + \hat{I}_z \hat{I}_x)\hat{\sigma}_z + (\hat{I}_y \hat{I}_z + \hat{I}_y \hat{I}_x)\hat{\sigma}_x \right] + \\
& Q_2 \left[(\hat{I}_y \hat{I}_y - \hat{I}_x \hat{I}_x)\hat{\sigma}_z + (\hat{I}_x \hat{I}_y + \hat{I}_y \hat{I}_x)\hat{\sigma}_x \right],
\end{aligned}
\tag{18}
$$

where S and $\{\hat{\sigma}_z = |^2E_x\rangle\langle^2E_x| - |^2E_y\rangle\langle^2E_y| = \left(\begin{smallmatrix} 1 & \\ & -1 \end{smallmatrix}\right)$, $\hat{\sigma}_x = |^2E_x\rangle\langle^2E_y| + |^2E_x\rangle\langle^2E_y| = \left(\begin{smallmatrix} & 1 \\ 1 & \end{smallmatrix}\right)\}$ depict the electron spin and orbital degrees of freedom, respectively. We show the hyperfine and quadrupolar parameters in Table III. We used the $(a_{1\uparrow}^1 a_{1\downarrow}^1 e_{x\uparrow}^{0.5} e_{y\uparrow}^{0.5} e_{x\downarrow}^0 e_{y\downarrow}^0)$ single electron occupation to determine the hyperfine parameters to avoid broken symmetry spin densities. However, the electric field gradient related to the nuclear quadrupole interaction does not depend on the broken symmetry spin density but rather on the local potential that is a scalar quantity. Therefore, in contrast to the calculation of hyperfine tensors, we use the broken symmetry occupation of Eq. (9) to determine the quadrupolar tensor of ^{14}N. By doing so the quadrupolar parameters become reduced upon removing the symmetry constraints from -5.2 MHz, 10.1 kHz, -11.0 kHz to -4.8 MHz, 9.6 kHz, -9.7 kHz for Q, Q_1, Q_2 matrix elements, respectively. However, the hyperfine parameters undergo an artificial change upon symmetry constraint removal: -2.8 MHz, -3.2 MHz, 0.1 MHz, -0.1 MHz parameters become 9.9 MHz, -6.3 MHz, 1.0 MHz, -0.8 MHz for $A_{\parallel}$, $A_{\perp}$, A_1, A_2, respectively, due to spin contamination error. Therefore, we use the symmetrical spin density results for hyperfine parameters in Table III for the sake of simplicity.

The dynamic JT also affects the hyperfine interaction of ^{13}C nuclear spins that might be present around the defect with 1.1% natural abundance in diamond. Three carbon atoms with dangling bonds near the vacancy exhibit the largest hyperfine couplings (see Fig. 4). The spin Hamiltonian for such states can be constructed[76] as follows,

$$
\hat{W} = \overleftrightarrow{S}\,\overleftrightarrow{A}\,\overrightarrow{I} + \overleftrightarrow{S}\,\overleftrightarrow{A}_x\,\overrightarrow{I}\,\hat{\sigma}_z + \overleftrightarrow{S}\,\overleftrightarrow{A}_y\,\overrightarrow{I}\,\hat{\sigma}_x, \tag{19}
$$

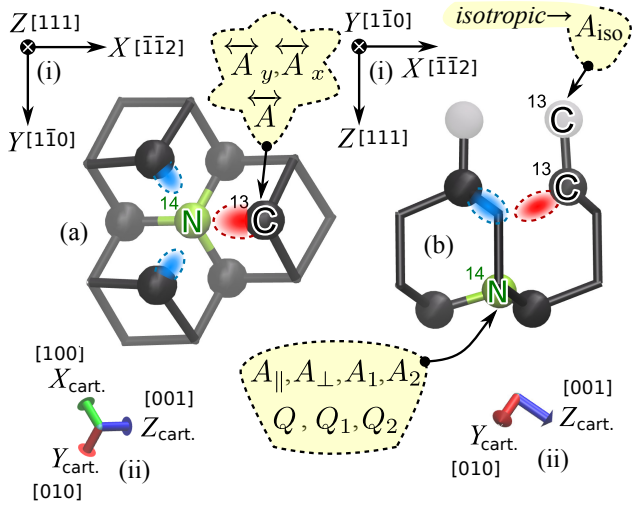

FIG. 4. Atomic positions of the NV^0 defect from two different orientations. We show two different viewing directions: (a) depicts the system viewed along the [111] trigonal symmetry axis while (b) depicts a viewing angle perpendicular to it. We depict the [111] oriented coordinate system in (i) used within Eqs. (18) and (20) for hyperfine and quadrupolar parameters larger than >1 MHz. Additionally, we show the Cartesian coordinate system of diamond in (ii). We depict the $|e_x\rangle$ orbital by the blue/red colors for negative/positive parts of the wavefunction.

where A is the symmetric part and A_x, A_y are the non-symmetric parts, and $\overleftarrow{S} = \left(\hat{S}_x \;\; \hat{S}_y \;\; \hat{S}_z\right)^{\mathrm{T}}$ and $\overrightarrow{I} = \left(\hat{I}_x \;\; \hat{I}_y \;\; \hat{I}_z\right)$ depict the electron and nuclear spin vectors, respectively. Similarly to that of the central ^{14}N nuclear spin, we determined the hyperfine matrices by means of HSE06 hybrid functional on the $(a^1_{1\uparrow}a^1_{1\downarrow}e^{0.5}_{x\uparrow}e^{0.5}_{y\uparrow}e^{0}_{x\downarrow}e^{0}_{y\downarrow})$ electronic configuration for which we report the following three

$$\overleftrightarrow{A} = \begin{pmatrix} 194 & 0 & 27 \\ 0 & 111 & 1 \\ 27 & 1 & 120 \end{pmatrix}, \quad \overleftrightarrow{A}_x = \begin{pmatrix} 51 & 2 & 12 \\ 2 & 12 & 1 \\ 12 & 1 & 16 \end{pmatrix}, \quad \overleftrightarrow{A}_y = \begin{pmatrix} -44 & 4 & -11 \\ 4 & -10 & 1 \\ -11 & 1 & -14 \end{pmatrix} \tag{20}$$

hyperfine matrices. We note that the carbon atoms with C−N bonds and all other 2nd, 3rd etc. neighbors exhibit negligible <1 MHz hyperfine constants except for the three equivalent carbon atoms that are connected to the carbon atoms with dangling bonds that we show in Fig. 4(b) with gray lobes. These three ^{13}C nuclear spins exhibit substantial isotropic hyperfine interaction ($\hat{W} = \overrightarrow{I}\, A_{\mathrm{iso}}\, \overleftarrow{S}$ effective Hamiltonian), e.g., only $\overleftrightarrow{A}$ is nonzero that of Eq. (20) and its diagonal is filled with the same $A_{\mathrm{iso}} = -10$ MHz parameter and all other parameters of Eq. (19) are less than 1 MHz.

D. Optical spectra between the doublet states

As mentioned in the Methods section (Sec. II), we determine the optical sidebands of PL and ABS spectra by means of the Huang-Rhys method[23,53]. First, we calculated the Huang-Rhys sideband by the geometry differences between the $\mathcal{A}|a^{\downarrow}_1 e^{\uparrow}_- e^{\uparrow}_+\rangle$ configuration and the $|^2E\rangle$ correlated ground state as depicted in Eq. (9) with all symmetry constraints lifted. However, the predicted $S = 1.16$ Huang-Rhys factor significantly underestimates the intensity of the PL sideband as plotted in Fig. 2(b).

Therefore, we utilize the correction scheme by means of Eq. (11) as follows. The derivatives against all X_i $(i = 3N-3)$ configuration coordinates

$$F_i\left(|^2A_2\rangle\right) = \frac{3}{2}\frac{\partial E_{tot}\left(\mathcal{A}|a^{\downarrow}_1 e^{\uparrow}_- e^{\uparrow}_+\rangle\right)}{\partial X_i} - \frac{1}{2}\frac{\partial E_{tot}\left(|^4A_2\rangle\right)}{\partial X_i} \tag{21}$$

gives an approximation for forces acting on nuclei for $|^2A_2\rangle$ state. In the case of linear electron-phonon coupling the forces are proportional to the relaxed atomic displacements [see Eq. (7) in Ref. 23]. Therefore, the optimized geometry of $|^2A_2\rangle$ can be estimated as

$$X_i\left(|^2A_2\rangle\right) = \frac{3}{2}X_i\left(|\mathcal{A}|a^{\downarrow}_1 e^{\uparrow}_- e^{\uparrow}_+\rangle\right) - \frac{1}{2}X_i\left(|^4A_2\rangle\right), \tag{22}$$

where $X_i(\Gamma)$ are relaxed atomic positions within electronic state Γ. We find that the correction scheme improves not only the ZPL energy (see Table I) it also predicts a PL sideband with $S = 1.91$ HR factor as depicted in Fig. 2(b).

The absorption spectrum is much broader than the PL spectrum for NV0 defect. We attribute this phenomenon to the presence of $|^2E^*\rangle$ second excited state close to the $|^2A_2\rangle$ first excited state. Furthermore, the ionization bands emerge at about 2.7 eV (e.g., Ref. 48) which overlaps with the phonon sideband of the $|^2A_2\rangle$ related absorption. In the next Section, we analyze the optical transition dipole moments towards the doublet excited states from the ground state.

E. Optical transition dipole moments

We determine the optical transition dipole moments between occupied-unoccupied Kohn-Sham state pairs as implemented in the VASP package[77]. For symmetry reasons, we placed half-half electrons on $|e^{\uparrow}_{x,y}\rangle$ orbitals of Fig. 1(a) thus populating the $(a^1_{1\uparrow}a^1_{1\downarrow}e^{0.5}_{x\uparrow}e^{0.5}_{y\uparrow}e^{0}_{x\downarrow}e^{0}_{y\downarrow})$ configuration to avoid broken symmetry solutions shown in Eq. (9). We calculate the transition dipole moments within the spin majority channel $|\langle a_{1\downarrow}|\hat{\boldsymbol{d}}|e_{x,y\downarrow}\rangle| = 4.22$ Debye and $|\langle e^{\uparrow}_x|\hat{\boldsymbol{d}}|e^{\uparrow}_y\rangle| = d'_{\perp}/\sqrt{2} = 1.81$ Debye. Next, we determine the transition dipole moments acting between multiplets of Eqs. (5), (7) and (10) as follows,

$$
\begin{aligned}
|\langle {}^2E_{\mp\frac{1}{2}}|\hat{\boldsymbol{d}}|^2A_2^{\pm}\rangle| &= |\langle {}^2E_{\pm\frac{3}{2}}|\hat{\boldsymbol{d}}|^2A_2^{\pm}\rangle| &&= c\sqrt{\tfrac{3}{2}}d_{\perp} &&= 4.36\ (5.17)\ \text{Debye},\\
|\langle {}^2E_{\pm\frac{1}{2}}|\hat{\boldsymbol{d}}|^2E^*_{\pm\frac{1}{2}}\rangle| &= |\langle {}^2E_{\mp\frac{3}{2}}|\hat{\boldsymbol{d}}|^2E^*_{\mp\frac{3}{2}}\rangle| &&= d_{\parallel} &&= 1.07\ \text{Debye},\\
|\langle {}^2E_{\mp\frac{1}{2}}|\hat{\boldsymbol{d}}|^2E^*_{\pm\frac{1}{2}}\rangle| &= |\langle {}^2E_{\mp\frac{3}{2}}|\hat{\boldsymbol{d}}|^2E^*_{\pm\frac{3}{2}}\rangle| &&= (c^2-d^2)d_{\perp}-cdd'_{\perp} &&= 0.62\ (4.36)\ \text{Debye},\\
|\langle {}^2E_{\mp\frac{1}{2}}|\hat{\boldsymbol{d}}|^2A_1^{\pm}\rangle| &= |\langle {}^2E_{\pm\frac{3}{2}}|\hat{\boldsymbol{d}}|^2A_1^{\pm}\rangle| &&= c\sqrt{\tfrac{1}{2}}d_{\perp} &&= 2.52\ (2.99)\ \text{Debye},
\end{aligned}
\tag{23}
$$

where we show the dipoles for $c = 0.84$ and $d = 0.54$ taking the correlation effects into account whereas the raw data without correlation ($c = 1.0$ and $d = 0.0$) are given in parentheses. Additionally, we give a rough estimate for $d_{\parallel}$ by determining the transition strength towards the [111] direction for the broken symmetry solution as given in Eq. (9). Therefore, we evaluate the dipole integral from the occupied $|ua_1^{\uparrow} + ve_x^{\uparrow}\rangle$ towards the unoccupied third spin-↑ orbital as $d_{\parallel} = 1.07$ Debye.

The radiative lifetime of dipole transitions ($\boldsymbol{d}$) can be evaluated[78] as $\tau = \frac{3\pi\varepsilon_0}{n\omega^3|\boldsymbol{d}|^2} = \frac{\alpha}{|\boldsymbol{d}|^2}$, where $n = 2.42$ is the refractive index of diamond, $\hbar\omega \approx 2.156$ eV is the excitation energy and ε_0 is the permittivity of vacuum. Finally, $\alpha = 501.15\ \frac{\text{Debye}^2}{\text{ns}}$ is the conversion factor from Debye to nanosecond units. This allows us to evaluate the radiative lifetimes as

$$
\tau({}^2A_2) = \frac{\alpha}{2\times c^2\frac{3}{2}d_{\perp}^2} = 6.6\ (4.7)\ \text{ns}, \tag{24a}
$$

$$
\tau({}^2E^*) = \frac{\alpha}{\left((c^2-d^2)d_{\perp}-cdd'_{\perp}\right)^2 + d_{\parallel}^2} = 164\ (14.1)\ \text{ns}, \tag{24b}
$$

where the data in parentheses are calculated by neglecting electronic correlation effects. We note that there is an extra $\frac{1}{2}$ factor for $\tau({}^2A_2)$ because $|{}^2E\rangle$ is double degenerate unlike $|{}^2A_2\rangle$.

The calculated 6.6 ns radiative lifetime overestimates the optical transition's strength as the experimentally observed excited state lifetime varies around 13-20 ns (Refs. 28–31). This result is surprising as our *ab initio* method correctly predicts radiative lifetime of NV^- excited state lifetime [13.7 ns in comparison to the experimentally observed 12.0 ns (Ref. 79)] by determining $d_{\perp}^{NV^-} = |\langle a_{1\downarrow}|\hat{\boldsymbol{d}}|e_{x,y\downarrow}\rangle| = 4.98$ Debye. We tentatively explain the discrepancy with the complex nature of the electronic excited states. We conclude from our *ab initio* calculations that the bright excited state of NV^0 does not have a pure $|{}^2A_2\rangle$ character because electron phonon-coupling can mix $|{}^2A_2\rangle$ and $|{}^2E^*\rangle$ excited states with each other as the two energy levels are very close to each other. In such a case if the coupling between them is strong it could also explain why the second ZPL for $|{}^2E^*\rangle$ is missing in ABS as the two electronic excited states are merged into common vibronic bands. The calculation of the electron-phonon coupling, i.e., the pseudo Jahn-Teller effect between $|{}^2A_2\rangle$ and $|{}^2E^*\rangle$ is beyond the scope of this study as it is extremely difficult to achieve a reliable adiabatic potential energy surfaces and energy spacing for the two excited state doublets at high accuracy.

In summary, we suggest polarization dependent measurements both for the sideband both in ABS and PL to resolve this issue. The optical polarization already been resolved for the ZPL absorption[80] that points to a $|{}^2E\rangle \leftrightarrow |{}^2A\rangle$ transition whereas later measurements confirmed[34] that the excited state is a $|{}^2A_2\rangle$ multiplet. In particular, an $|{}^2A_2\rangle$ multiplet active through "x" and "y" directional $d_{\perp}$ dipoles only whereas $|{}^2E^*\rangle$ additionally active through the $d_{\parallel}$ dipole pointing towards "z". However, we propose that the optical sidebands contain not only the $|{}^2A_2\rangle$ character thus "z" dipole activity should be present towards the $|{}^2E^*\rangle$ multiplet at higher energies in the absorption spectrum. The variation of the observed optical lifetimes of NV^0 with various excitation techniques in bulk diamond might be also explained by the intertwined $|{}^2A_2\rangle$ and $|{}^2E^*\rangle$ character of the excited state.

V. LIFETIME OF $|{}^4A_2\rangle$ METASTABLE STATE

The $|{}^4A_2\rangle$ is an orbitally non-degenerate state, thus the spin-orbit interaction is zero within $|{}^4A_2\rangle$ but it could occur between the doublets and $|{}^4A_2\rangle$ as a second order interaction. The only doublet state close in energy is the ground state $|{}^2E\rangle$ whereas the other states can be ignored because of large energy spacing. We introduce the SOC matrix elements between orbitals that are responsible for ISC. First, we determine the possible SOC matrix elements that connect $|{}^4A_2\rangle$ to the ground state. One may notice that only the (aae) configuration of $|{}^2E\rangle$ is connected by SOC, i.e., $\langle {}^4A_2|\hat{H}_{\text{SOC}}|{}^2E'\rangle \neq 0$ because the $\langle {}^4A_2|\hat{H}_{\text{SOC}}|{}^2E''\rangle = 0$ for (aee) configuration as two-particle excitation would be required to transform $(ae_{\pm}e_{\mp})$ configuration into $(ae_{\pm}e_{\pm})$, c.f. Eqs. (1) and (6) for details. Therefore the SOC matrix elements are

$$
\begin{aligned}
|\langle {}^4A_2^{\pm\frac{3}{2}}|\hat{H}_{\text{SOC}}|{}^2E_{\pm\frac{3}{2}}\rangle| &= |c\langle a_1^{\downarrow}|\hat{h}_{\text{SOC}}|e_{-}^{\uparrow}\rangle| &&= \sqrt{2}c\lambda_{\perp},\\
|\langle {}^4A_2^{\pm\frac{1}{2}}|\hat{H}_{\text{SOC}}|{}^2E_{\pm\frac{1}{2}}\rangle| &= |c\tfrac{1}{\sqrt{3}}\langle a_1^{\downarrow}|\hat{h}_{\text{SOC}}|e_{-}^{\uparrow}\rangle| &&= \sqrt{\tfrac{2}{3}}c\lambda_{\perp},\\
|\langle {}^2A_2|\hat{H}_{\text{SOC}}|{}^2E_{\pm\frac{1}{2}}\rangle| &= |c\tfrac{1}{\sqrt{6}}\langle a_1^{\downarrow}|\hat{h}_{\text{SOC}}|e_{-}^{\uparrow}\rangle| &&= \tfrac{1}{\sqrt{3}}c\lambda_{\perp},\\
|\langle {}^2A_1|\hat{H}_{\text{SOC}}|{}^2E_{\pm\frac{1}{2}}\rangle| &= |c\tfrac{1}{\sqrt{2}}\langle a_1^{\downarrow}|\hat{h}_{\text{SOC}}|e_{-}^{\uparrow}\rangle| &&= c\lambda_{\perp}.
\end{aligned}
\tag{25}
$$

The first two equations in Eq. (25) are important to consider in the context. To summarize, in terms of electronic structure, the relaxation into $|E_{\frac{3}{2}}\rangle$ is thrice faster than that into $|E_{\frac{1}{2}}\rangle$. Next, we use the HR theory as described

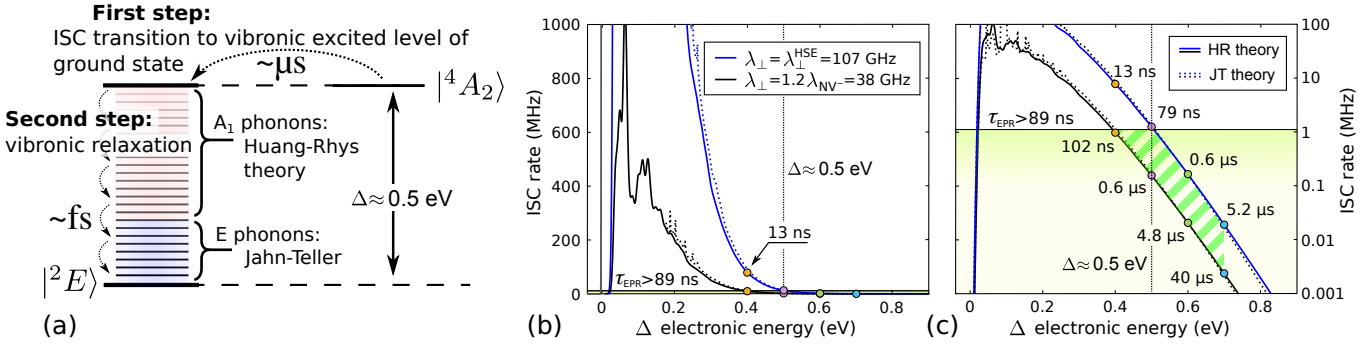

FIG. 5. Intersystem crossing (ISC) from the metastable $^4A_2$ state of NV^0 defect. (a) Mechanism of the ISC process. (b) and (c) ISC process within linear and log scale, respectively. We depict the theoretically viable region by green stripes in (c). We take an upper bound for the ISC rate (τ_{EPR}^{-1}) from EPR measurements (Ref. 38, see Sec. V for details).

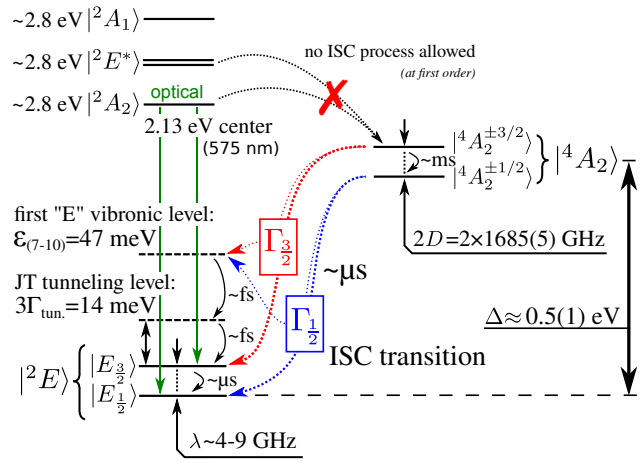

FIG. 6. Summary of ISC rates and level structure of NV^0. We take the experimentally observed D zero-field splitting value from Ref. 38. Additionally, we expect that $|^4A_2\rangle$ spin relaxation time is close to that of $|^3A_2\rangle$ of NV^- because both multiplets are similar orbital singlets.

in Refs. 24, 79, 81–83 to determine the ISC rates that can be expressed as

$$\begin{aligned}\Gamma_{\frac{3}{2}} &= I\left({}^4A_2^{\pm\frac{3}{2}} \rightarrow E_{\pm\frac{3}{2}}\right) = 4\pi\hbar c^2\lambda_\perp^2 F(\Delta)\\ \Gamma_{\frac{1}{2}} &= I\left({}^4A_2^{\pm\frac{1}{2}} \rightarrow E_{\pm\frac{1}{2}}\right) = \tfrac{4}{3}\pi\hbar c^2\lambda_\perp^2 F(\Delta)\end{aligned} \quad (26)$$

where F is the Huang-Rhys spectral function between $|^4A_2\rangle$ and $|^2E\rangle$ levels and Δ is the energy difference between the two levels. We obtained F function by relaxing the atomic positions within $|^4A_2\rangle$ and $|^2E\rangle$ configurations. We note that initially we applied C_{3v} symmetry constraint on the geometry of the DFT calculation that results in HR factor S_{A_1}=0.90 from totally symmetric (A_1) modes. When we removed all symmetry constraints and relaxed to the JT minimum in Fig. 3 the HR factor increased to S=S_{A_1}+S_E=1.53 that includes the additional effect of E phonons that we depict the resulting $F_{HR}(\hbar\omega)$ in Fig. 5 graphically.

Additionally, we determine the spectral function for ISC by means of JT theory: $F(\hbar\omega)=\sum_i^\infty c_{0,(i)}^2 F_{A_1}(\hbar\omega-\varepsilon_i)$ where $F_{A_1}(\hbar\omega)$ is the HR spectral function exhibiting S_{A_1}=0.90 HR factor and ε_i/Ψ_i is the eigenspectrum/wavefuncion of JT Hamiltonian of Eq. (14). At zero temperature there would be no E-phonons present within the metastable quartet thus its electronic plus E_x-E_y-phonon wavefunction would be a $\langle{}^4A_2|\otimes\langle 0,0|$ vacuum state for vibrations. Any $|\Psi_i\rangle$ can be expressed as $|\Psi_i\rangle = c_{00}^{(i)}|^2E_{m_j}\rangle\otimes|0,0\rangle + \sum_{n,m,m'_j}^{n+m\geq 1} c_{n,m,m'_j}^{(i)}|^2E_{m'_j}\rangle\otimes|n,m\rangle$ within the Born-Oppenheimer basis, where $|n,m\rangle = \frac{(a_X^\dagger)^n(a_Y^\dagger)^m}{\sqrt{n!m!}}|0,0\rangle$. Therefore, it can be concluded that the ISC process cannot target $|\Psi_i\rangle$ JT levels transforming as A_1 or A_2 representations because their $c_{00}^{(i)}$ expansion coefficient is zero due to group theory constraints and $|n,m\rangle$s are thermally not activated. ISC towards to the lowermost four $|^2E_{m_j}\rangle$ relaxes with the $c_{00(1-4)}^2=0.516$ coefficient and m_j is conserved fully from the initial $|^4A_2\rangle$. However, if the system relaxes to the first vibronic E-level ($|\Psi_{1-4}\rangle$) at ε_{7-10} = 47 meV firstly by $c_{00(7-10)}^2$ = 0.280 coefficient a very fast relaxation will occur back to $|^2E_{m_j}\rangle$ or towards the $|\Psi_{5-6}\rangle$ JT tunneling state at $\varepsilon_{5-6}=3\Gamma_{tun.}$ = 14 meV. We note that here $m_j=\pm\frac{1}{2}\leftrightarrow\mp\frac{3}{2}$ transfers are allowed and we expect that orbital relaxation[84] would be the dominating process in ~fs region[85]. Nevertheless, the system would relax to $|^2E_{\pm\frac{1}{2}}\rangle$ from $|^2E_{\mp\frac{3}{2}}\rangle$ within ~μs due to the same orbital relaxation.

Surprisingly, the correction from JT theory is negligible. We calculated the ISC process fully by means of HR theory only: $F(\hbar\omega)\approx F_{HR}(\hbar\omega)=\int F_{A_1}(\varepsilon)F_E(\hbar\omega-\varepsilon)d\varepsilon$ we obtained almost the same transition rate as that of JT theory [see Fig. 5(c)]. We used two estimates for $\lambda_\perp$. Firstly, we used our $\lambda_\perp$ = 107.3 GHz *ab initio* result as we discussed in Sec. IV B. However, our previous study about ISC processes for NV^- indicated that the off-diagonal SOC matrix elements may overestimate[24,82] the strength of the transition. Therefore, we used the previous result only as an upper bound and we used $\lambda_\perp = 1.2\times\lambda_z^{NV^-}$ where $\lambda_z^{NV^-}$ is the SOC parameter

of NV^- in its $|^3E\rangle$ excited state as suggested by previous studies[24,79,81,82]. Finally, we use the HSE06 $c^2 = 0.71$ correlation parameter as discussed in Sec. III B. We note that HSE06 DFT usually predicts the position non-correlated states within ± 0.1 eV precision. Therefore, we estimate the position of $|^4A_2\rangle$ level as 0.48 ± 0.1 eV (see Table I). However, we note that configurational interaction wavefunction methods predict $|^4A_2\rangle$ at 0.68 eV so we use 0.7 eV as an upper bound for Δ. Therefore, all the necessary parameters are known to evaluate Eq. (26). By taking all the broad energy intervals into account, our theory predicts the lifetime of $|^4A_2^{\pm\frac{1}{2}}\rangle$ within 40 μs$-$13 ns within the $\Delta = 0.7$ eV$\ldots$0.4 eV interval (see Table I).

An another aspect of $|^4A_2\rangle$ is that it is EPR active. As we mentioned in the introduction it can be occupied with ionizing NV^-. However, the ISC rate cannot be too fast otherwise the optically induced EPR could not be observed. Indeed, we fitted Lorentzian peaks on the first top-left experimentally measured EPR spectra from Fig. 1(a) in Ref. 38 recorded at $T = 10$ K. We estimated the linewidth of the Lorentzian broadening as 0.068(3) mT that corresponds to 1.8(1) MHz in EPR frequency. Therefore, we can interpret the linewidth as natural line broadening to estimate the spin lifetime of $|^4A_2\rangle$ as $\tau_{\rm EPR} \gtrapprox \frac{1}{2\pi\times 1.8\,\rm MHz} = 89(3)$ ns. However, the broadening may arise from other sources such as hyperfine interaction broadening due to distant ^{13}C isotopes for example. Thus, we use this value only as a minimum estimation for $\Gamma_{\frac{1}{2}}^{-1}$ [see the green area in Figs. 5(b) and (c)]. Our final conclusion is that the lifetime of $|^4A_2\rangle$ is in the μs regime at cryogenic temperatures. We summarize the level structure of NV^0 and the possible transitions in Fig. 6. It is worthy to consider the route on which the system may end up in $|^4A_2\rangle$. However, it can be seen that the $|^4A_2\rangle$ is separated from $|^2A_2\rangle$ by 1.6 eV, thus ISC transition is negligible between the states. Therefore, in the next Section we will present how photoionization of NV^- can populate the metastable spin quartet state, $|^4A_2\rangle$.

VI. PHOTOIONIZATION OF NV DEFECT

The NV defect is often observed under illumination. The most typical photoexcitation of NV defect occurs with green laser (e.g., at 532 nm in wavelength or 2.33 eV in energy) which can lead to charge switching between the negatively charged and neutral NV defects.

Understanding of photoionization of NV defect is difficult because of the possible non-linear optical effects such as successive two-photon absorption processes via real excited states and the presence of long-living $|^1E\rangle$ in NV^- and $|^4A_2\rangle$ in NV^0. It is very challenging to calculate the photoionization threshold energies and rates at *ab initio* level for two reasons: (i) the singlet states in NV^- cannot be accurately calculated by DFT and (ii) simple ionization and Auger-ionization might compete where the latter is a two-body interaction, an inherently complex task for *ab initio* methods. Issue (i) can be principally solved by embedding wavefunction techniques that was applied to the ionization of $|^1E\rangle$ of NV^-[86]. We note that the photoionization cross-section in that study was calculated within the Γ-point in a 512-atom supercell which is not fully convergent because the continuous band region at elevated energies above the ionization threshold energy requires much higher k-point sampling[87] and band unfolding methods[42]. Nevertheless, the calculated photoionization threshold energy at 2.2 eV implies that direct ionization, $NV^-+h\nu\rightarrow NV^0+e^-_{\rm CBM}$, occurs under green illumination. Issue (ii) was dealt with representing the appropriate exciton wavefunctions by combination of the respective Kohn-Sham wavefunctions in the Coulomb-integrals associated with the Auger-ionization rates[88]. The method was applied to the $|^3E\rangle$ of NV^- ionization to the ground state of NV^0 and resulted in about 1 ns inverse rate[88]. This result was later criticized with the argument that the electron density in the applied 512-atom supercell was very high so the Auger-ionization rate was orders of magnitude overestimated which should depend on the carriers density[42]. On the other hand, no other *ab initio* data has been yet published about the Auger-ionization rates of NV defect to justify this argument.

In this study we proved that even the ground state of NV^0 is highly correlated that was not considered in the previous studies in the context of photoionization cross-section. Because of the high complexity of the multiplet states of NV^0 and numerical challenges of calculating direct and Auger-ionization rates, we rather show the estimated photoionization threshold energies for the $NV^-+h\nu\rightarrow NV^0+e^-_{\rm CBM}$ and $NV^0+h\nu\rightarrow NV^-+h^-_{\rm VBM}$ processes (see Fig. 7). Furthermore, we use the Slater-Condon principles to identify the feasible ionization processes as alluded in Refs. 42 and 89 for $NV^-+h\nu\rightarrow NV^0+e^-_{\rm CBM}$ and $NV^0+h\nu\rightarrow NV^-+h^-_{\rm VBM}$, respectively. Briefly, Slater-Condon selection rule implies that direct ionization and Auger-ionization only occurs for changing maximum one and two single particle wavefunctions between the initial and final multiplet states, respectively.

We start with the simplest photoionization scheme, i.e., the single photon absorption from initial ground state to final ground state. This yields $|^3A_2\rangle + 2.6\,\rm eV \rightarrow |^2E\rangle$ and $|^2E\rangle + 2.8\,\rm eV \rightarrow |^3A_2\rangle$ where the first process was observed at room temperature[90] for which the $T = 0$ K DFT calculation predicted 2.7 eV[48,87]. These energies fall the blue wavelength region. We note that the ground state $|^2E\rangle$ is a correlated multiplet (see Eq. (10)) of 71% $|^2E'\rangle$ character, so the direct ionization process is partially quenched as Slater-Condon selection rule prohibits the direct ionization towards $|^2E''\rangle$ with 28% contribution to the $|^2E\rangle$ ground state of NV^0 that we depict by dashed arrows in Fig. 7. On the hand, the shelving state of NV^-, $|^1E\rangle$, can be ionized by green light as $|^1E\rangle + 2.2\,\rm eV \rightarrow |^2E\rangle$ where no quenching occurs

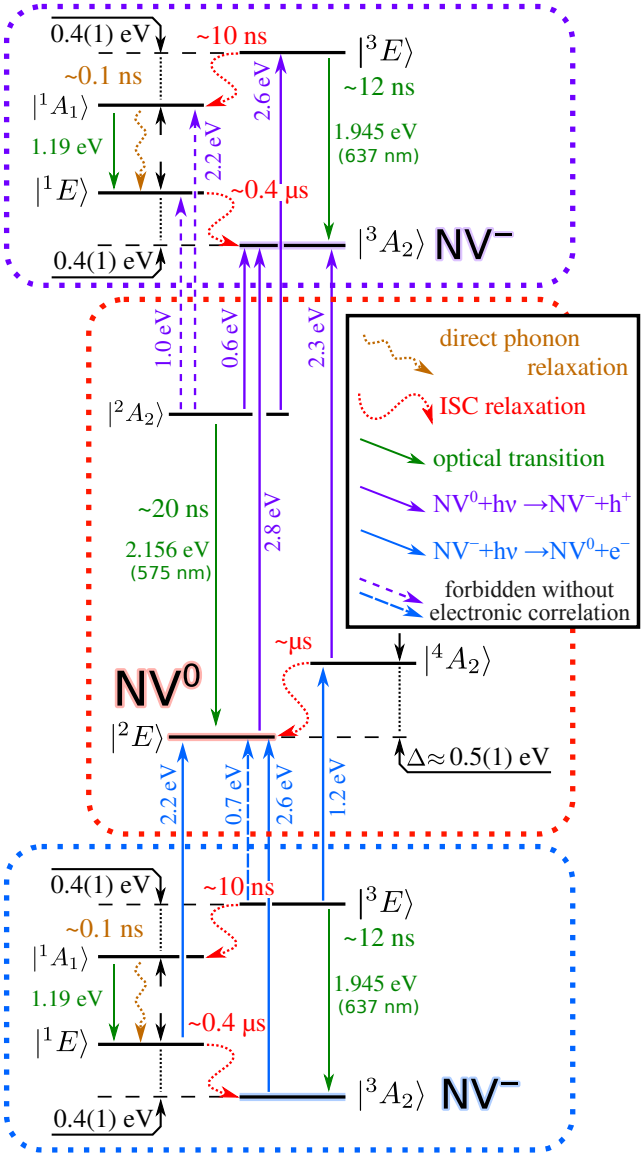

FIG. 7. Summary of photoionization processes of NV^0. We round the related transition rates, thus we depict the lifetimes as rough ps, ns, and μs estimates.

due to the correlated nature of $|^2E\rangle$. We find that the shelving state of NV^0, $|^4A_2\rangle$, behaves very similarly as $|^4A_2\rangle + 2.3\,\text{eV} \rightarrow |^3A_2\rangle$ which is fully allowed by direct ionization process. Finally, we note that ionization from $|^1A_1\rangle$ is unlikely due to its very short lifetime of 100 ps[91].

As was also pointed out in Ref. 42, intersystem crossing is strongly hindered between $|^2A_2\rangle$ and $|^4A_2\rangle$ because of selection rules and a large energy spacing between these levels so occupation of the shelving $|^4A_2\rangle$ could occur via photoionization from NV^-. Direct ionization from $|^3A_2\rangle$ yields an ultraviolet threshold energy for this process but then it would immediately convert it back to NV^-. However, it was found in an EPR measurement[38] that green illumination for NV ensemble diamond samples can effectively pump the system into $|^4A_2\rangle$. This may be explained two-photon absorption from $|^3A_2\rangle$ to $|^4A_2\rangle$ via $|^3E\rangle$. In this process, the first photon is absorbed to go from $|^3A_2\rangle$ to $|^3E\rangle$ (usual neutral excitation) and the second photon is quickly absorbed before it decays within NV^-. In Ref. 42 they argued that Slater-Condon rules dictate that direct ionization occurs only towards $|^4A_2\rangle$ with a threshold energy at 1.2 eV which explains the enhancement of ionization at this energy in a two-color excitation experiment[92]. Furthermore, it could also explain a spinpolarization of the $|^4A_2\rangle$ towards $m_s = \pm\frac{1}{2}$ over $m_s = \pm\frac{3}{2}$[42]. Indeed, this phenomenon can be observed in Fig. 1(b) of Ref. 38 where the $-\frac{3}{2} \leftrightarrow -\frac{1}{2}$ transition (1st spectrum) exhibits induced emission (positive Lorentzian) whereas the $+\frac{1}{2} \leftrightarrow +\frac{3}{2}$ transition (4th spectrum) can be identified as absorption (negative Lorentzian). Our analysis shows that the lifetime of $|^4A_2\rangle$ can be indeed μs long in dark once the state has been occupied. However, green illumination can photoionize it back to the ground state of NV^- according to our results. Thus, this is a rather complex process where the average lifetime of $|^4A_2\rangle$ depends on many factors, e.g., the laser power and the presence of other defects that may induce additional carriers (electrons and holes) upon illumination.

We analyze further the two-photon ionization processes. Our calculations on NV^0 revealed that direct ionization channel exists between $|^3E\rangle$ and $|^2E\rangle$ because of the 28% $|^2E''\rangle$ character in the latter. Thus, an additional direct ionization process occurs from 0.7 eV from $|^3E\rangle$ beside the already considered $|^3E\rangle + 1.2\,\text{eV} \rightarrow |^4A_2\rangle$ process in Ref. 42. The Auger-ionization process from $|^3E\rangle$ is fully active towards $|^2E\rangle$. Thus, the sum of direct ionization and Auger-ionization rates will give the total ionization rate. Next we consider the two-photon ionization processes via $|^2A_2\rangle$. The $|^2A_2\rangle + 0.6\,\text{eV} \rightarrow |^3A_2\rangle$ process is very similar to the reverse ionization process where this process is partially quenched by the electron-phonon related mixture of $|^2E^*\rangle$ into $|^2A_2\rangle$ similarly to that of the quenched radiative lifetime of $|^2A_2\rangle$ (see Sec. IV E). Additionally, the $|^2A_2\rangle + 1.0\,\text{eV} \rightarrow |^1E\rangle$ process is also forbidden at linear order at Slater-Condon level. However, it becomes partially allowed due the electron-phonon related mixture of $|^2E^*\rangle$ or the correlated nature of $|^1E\rangle$ (see Ref. 82). We note again that Auger-ionization process is fully allowed between these two states. Auger-ionization also can connect the $|^2A_2\rangle$ and $|^2A_1\rangle$ multiplets and direct ionization is only allowed in second order since it requires $|^2E''\rangle$ character to be mixed in that is only possible though simultaneous electron-phonon interaction and electronic correlation effects within $|^2A_2\rangle$. We argued in a previous study[89] that the Auger-ionization rate can be substantial because of the presence of a deep resonant defect state of NV^0 in the valence band, thus we argue that $|^2A_2\rangle + 2.2\,\text{eV} \rightarrow |^1A_1\rangle$ indeed occurs[89]. Finally, ionization may occur from $|^2A_2\rangle$ towards $|^3E\rangle$ upon blue illumination starting at 2.6 eV, thus this route is blocked at the typical green illumination of NV defect.

VII. SUMMARY

The electronic structure of NV^0 was determined by DFT HSE06 calculations where the correlation of orbitals are taken into account with the guide of group theory, in order to induce correction in the total energy and the geometry in the excited states. We find that the electron-phonon coupling is very strong that affects both the fine structure of the ground state as well as the radiative lifetime of the excited state. In particular, we find that the ^2E and $^2A_2$ excited states are intertwined by symmetry breaking phonons and the optical properties can be only explained by invoking strong electron-phonon coupling between the doublet excited states. We also analyzed the lifetime of the $^4A_2$ metastable state and provided a detailed analysis on the intersystem crossing between the metastable quartet state and the doublet ground state. Finally, the calculated electronic structure of NV^0 yields new insights about the photoionization processes of NV defect.

ACKNOWLEDGMENTS

We thank L. Razinkovas, R. Ulbricht, C. Linderälv for fruitful discussions. Support by the National Research, Development and Innovation Office (NKFIH) as well as by the Ministry of Culture and Innovation within the Quantum Information National Laboratory of Hungary (Grant No. 2022-2.1.1-NL-2022-00004) is much appreciated. AG acknowledges the high-performance computational resources provided by KIFÜ (Governmental Agency for IT Development) institute of Hungary, the European Commission for the projects QuMicro (Grant No. 101046911) and SPINUS (Grant No. 101135699) and the QuantERA II project Maestro (NKFIH Grant No. 2019-2.1.7-ERA-NET-2022-00045).

* thiering.gergo@wigner.hun-ren.hu
† gali.adam@wigner.hun-ren.hu

[1] L. du Preez, Ph.D. thesis, University of Witwatersrand, Johannesburg (1965).
[2] M. W. Doherty, N. B. Manson, P. Delaney, F. Jelezko, J. Wrachtrup, and L. C. Hollenberg, Physics Reports **528**, 1 (2013).
[3] A. Gruber, A. Drabenstedt, C. Tietz, L. Fleury, J. Wrachtrup, and C. v. Borczyskowski, Science **276**, 2012 (1997), http://www.sciencemag.org/cgi/reprint/276/5321/2012.pdf.
[4] F. Jelezko, T. Gaebel, I. Popa, A. Gruber, and J. Wrachtrup, Phys. Rev. Lett. **92**, 076401 (2004).
[5] T. D. Ladd, F. Jelezko, R. Laflamme, Y. Nakamura, C. Monroe, and J. L. O'Brien, Nature **464**, 45 (2010).
[6] D. D. Awschalom, L. C. Bassett, A. S. Dzurak, E. L. Hu, and J. R. Petta, Science **339**, 1174 (2013).
[7] A. Gali, Nanophotonics **8**, 1907 (2019).
[8] M. Pompili, S. L. N. Hermans, S. Baier, H. K. C. Beukers, P. C. Humphreys, R. N. Schouten, R. F. L. Vermeulen, M. J. Tiggelman, L. dos Santos Martins, B. Dirkse, S. Wehner, and R. Hanson, Science **372**, 259 (2021).
[9] V. Acosta and P. Hemmer, MRS Bulletin **38**, 127 (2013).
[10] K. Jensen, N. Leefer, A. Jarmola, Y. Dumeige, V. Acosta, P. Kehayias, B. Patton, and D. Budker, Physical Review Letters **112** (2014), 10.1103/physrevlett.112.160802.
[11] S. I. Bogdanov, M. Y. Shalaginov, A. S. Lagutchev, C.-C. Chiang, D. Shah, A. S. Baburin, I. A. Ryzhikov, I. A. Rodionov, A. V. Kildishev, A. Boltasseva, and V. M. Shalaev, Nano Letters **18**, 4837 (2018).
[12] M. Gulka, D. Wirtitsch, V. Ivády, J. Vodnik, J. Hruby, G. Magchiels, E. Bourgeois, A. Gali, M. Trupke, and M. Nesladek, Nature Communications **12** (2021), 10.1038/s41467-021-24494-x.
[13] A. Gali, Phys. Rev. B **79**, 235210 (2009).
[14] M. S. Barson, E. Krausz, N. B. Manson, and M. W. Doherty, Nanophotonics **8**, 1985 (2019).
[15] Z. Su, Z. Ren, Y. Bao, X. Lao, J. Zhang, J. Zhang, D. Zhu, Y. Lu, Y. Hao, and S. Xu, Journal of Materials Chemistry C **7**, 8086 (2019).
[16] S. Baier, C. E. Bradley, T. Middelburg, V. V. Dobrovitski, T. H. Taminiau, and R. Hanson, Phys. Rev. Lett. **125**, 193601 (2020).
[17] Y.-F. Gao, J.-M. Lai, Y.-J. Sun, X.-L. Liu, C.-N. Lin, P.-H. Tan, C.-X. Shan, and J. Zhang, ACS Photonics **9**, 1605–1613 (2022).
[18] C. D. Clark and C. A. Norris, Journal of Physics C: Solid State Physics **4**, 2223 (1971).
[19] G. Davies and M. F. Hamer, Proceedings of the Royal Society A: Mathematical, Physical and Engineering Sciences **348**, 285 (1976).
[20] P. Kehayias, M. W. Doherty, D. English, R. Fischer, A. Jarmola, K. Jensen, N. Leefer, P. Hemmer, N. B. Manson, and D. Budker, Physical Review B **88**, 165202 (2013).
[21] G. Davies, Journal of Physics C: Solid State Physics **12**, 2551 (1979).
[22] N. Manson and J. Harrison, Diamond and Related Materials **14**, 1705 (2005).
[23] A. Alkauskas, B. B. Buckley, D. D. Awschalom, and C. G. V. de Walle, New Journal of Physics **16**, 073026 (2014).
[24] G. Thiering and A. Gali, Physical Review B **96**, 081115 (2017).
[25] L. Razinkovas, M. W. Doherty, N. B. Manson, C. G. Van de Walle, and A. Alkauskas, Phys. Rev. B **104**, 045303 (2021).
[26] See Fig. 5.81. in Ref. **?** where the temperature dependent Debye-Waller (DW) factor is approximately DW ∼0.095 at $T \sim 77$ K that translates into $S = -\ln \mathrm{DW} \approx 2.35$ HR factor. Original (unpublished) work is in Ref. **?** .
[27] K. Wang, J. W. Steeds, Z. Li, and Y. Tian, Microscopy and Microanalysis **22**, 108 (2016).
[28] N. Mizuochi, T. Makino, H. Kato, D. Takeuchi, M. Ogura, H. Okushi, M. Nothaft, P. Neumann, A. Gali, F. Jelezko, J. Wrachtrup, and S. Yamasaki, Nature Photonics **6**, 299 (2012).
[29] G. Liaugaudas, G. Davies, K. Suhling, R. U. A. Khan, and D. J. F. Evans, Journal of Physics: Condensed Matter **24**,

435503 (2012).
[30] D. Gatto Monticone, F. Quercioli, R. Mercatelli, S. Soria, S. Borini, T. Poli, M. Vannoni, E. Vittone, and P. Olivero, Phys. Rev. B **88**, 155201 (2013).
[31] E. Fraczek, V. G. Savitski, M. Dale, B. G. Breeze, P. Diggle, M. Markham, A. Bennett, H. Dhillon, M. E. Newton, and A. J. Kemp, Opt. Mater. Express **7**, 2571 (2017).
[32] P. Sáenz de Santa María Modroño and G. Jacopin, "NV centers in diamond as a CL temperature probe, Poster at hasselt diamond workshop 2024 - SBDD XXVIII." (2024).
[33] N. B. Manson, M. Hedges, M. S. J. Barson, R. Ahlefeldt, M. W. Doherty, H. Abe, T. Ohshima, and M. J. Sellars, New Journal of Physics **20**, 113037 (2018).
[34] N. B. Manson, K. Beha, A. Batalov, L. J. Rogers, M. W. Doherty, R. Bratschitsch, and A. Leitenstorfer, Phys. Rev. B **87**, 155209 (2013).
[35] A. Batalov, V. Jacques, F. Kaiser, P. Siyushev, P. Neumann, L. J. Rogers, R. L. McMurtrie, N. B. Manson, F. Jelezko, and J. Wrachtrup, Phys. Rev. Lett. **102** (2009), 10.1103/physrevlett.102.195506.
[36] L. C. Bassett, F. J. Heremans, D. J. Christle, C. G. Yale, G. Burkard, B. B. Buckley, and D. D. Awschalom, Science **345**, 1333 (2014).
[37] Note that $2\lambda\hat{L}_z\hat{S}_z$ spin-orbit coupling operator were defined in Refs. 14 and 16 whereas we define the spin-orbit coupling as $\lambda\hat{l}_z\hat{s}_z = \frac{\lambda}{2}\big(|e^{\uparrow}_{+}\rangle\langle e^{\uparrow}_{+}| + |e^{\downarrow}_{-}\rangle\langle e^{\downarrow}_{-}| - |e^{\downarrow}_{+}\rangle\langle e^{\downarrow}_{+}| - |e^{\uparrow}_{-}\rangle\langle e^{\uparrow}_{-}|\big)$.
[38] S. Felton, A. M. Edmonds, M. E. Newton, P. M. Martineau, D. Fisher, and D. J. Twitchen, Phys. Rev. B **77** (2008), 10.1103/physrevb.77.081201.
[39] A. Norambuena, A. Jimenez, C. Becher, and J. R. Maze, New J. Phys. **22**, 073068 (2020).
[40] A. Ranjbar, M. Babamoradi, M. H. Saani, M. A. Vesaghi, K. Esfarjani, and Y. Kawazoe, Physical Review B **84**, 165212 (2011).
[41] W. Pfäffle, D. Antonov, J. Wrachtrup, and G. Bester, Phys. Rev. B **104**, 104105 (2021).
[42] L. Razinkovas, M. Maciaszek, F. Reinhard, M. W. Doherty, and A. Alkauskas, Phys. Rev. B **104**, 235301 (2021).
[43] G. Kresse and J. Furthmüller, Phys. Rev. B **54**, 11169 (1996).
[44] P. E. Blöchl, Phys. Rev. B **50**, 17953 (1994).
[45] O. Bengone, M. Alouani, P. Blöchl, and J. Hugel, Phys. Rev. B **62**, 16392 (2000).
[46] J. Heyd, G. E. Scuseria, and M. Ernzerhof, The Journal of Chemical Physics **118**, 8207 (2003).
[47] A. V. Krukau, O. A. Vydrov, A. F. Izmaylov, and G. E. Scuseria, The Journal of Chemical Physics **125**, 224106 (2006).
[48] P. Deák, B. Aradi, T. Frauenheim, E. Janzén, and A. Gali, Phys. Rev. B **81**, 153203 (2010).
[49] A. Alkauskas, M. D. McCluskey, and C. G. V. de Walle, J. Appl. Phys. **119**, 181101 (2016).
[50] A. Gali, Phys. Rev. B **80**, 241204 (2009).
[51] G. Thiering and A. Gali, Phys. Rev. X **8** (2018), 10.1103/physrevx.8.021063.
[52] G. Thiering and A. Gali, Phys. Rev. Research **3** (2021), 10.1103/physrevresearch.3.043052.
[53] K. Huang and A. Rhys, Proceedings of the Royal Society A: Mathematical, Physical and Engineering Sciences **204**, 406 (1950).
[54] See Supplemental Material in Ref. **?** .
[55] J. P. Perdew, K. Burke, and M. Ernzerhof, Phys. Rev. Lett. **77**, 3865 (1996).
[56] S. Steiner, S. Khmelevskyi, M. Marsmann, and G. Kresse, Phys. Rev. B **93** (2016), 10.1103/physrevb.93.224425.
[57] V. Ivády, I. A. Abrikosov, and A. Gali, npj Comput Mater **4** (2018), 10.1038/s41524-018-0132-5.
[58] A. Csóré and A. Gali, Phys. Rev. B **102** (2020), 10.1103/physrevb.102.241201.
[59] J. P. Goss, R. Jones, S. J. Breuer, P. R. Briddon, and S. Öberg, Phys. Rev. Lett. **77**, 3041 (1996).
[60] M. Łuszczek, R. Laskowski, and P. Horodecki, Physica B: Condensed Matter **348**, 292 (2004).
[61] J. A. Larsson and P. Delaney, Physical Review B **77**, 165201 (2008).
[62] C.-K. Lin, Y.-H. Wang, H.-C. Chang, M. Hayashi, and S. H. Lin, The Journal of Chemical Physics **129**, 124714 (2008).
[63] A. Gali, M. Fyta, and E. Kaxiras, Physical Review B **77**, 155206 (2008).
[64] P. Delaney, J. C. Greer, and J. A. Larsson, Nano Letters **10**, 610 (2010).
[65] Y. Ma, M. Rohlfing, and A. Gali, Physical Review B **81**, 041204 (2010).
[66] S. Choi, M. Jain, and S. G. Louie, Phys. Rev. B **86**, 041202 (2012).
[67] J. R. Maze, A. Gali, E. Togan, Y. Chu, A. Trifonov, E. Kaxiras, and M. D. Lukin, New Journal of Physics **13**, 025025 (2011).
[68] M. W. Doherty, N. B. Manson, P. Delaney, and L. C. L. Hollenberg, New Journal of Physics **13**, 025019 (2011).
[69] U. von Barth, Physical Review A **20**, 1693–1703 (1979).
[70] G. Thiering and A. Gali, Physical Review B **94** (2016), 10.1103/physrevb.94.125202.
[71] I. Bersuker, *The Jahn-Teller effect* (Cambridge University Press, 2006).
[72] I. Bersuker and V. Polinger, *Vibronic interactions in molecules and crystals*, Vol. 49 (Springer Science & Business Media, 2012).
[73] J. Zhang, C.-Z. Wang, Z. Zhu, Q. H. Liu, and K.-M. Ho, Phys. Rev. B **97**, 165204 (2018).
[74] Spherical harmonics are not compatible with the $|e_{\pm}\rangle = [|e_x\rangle \pm i|e_y\rangle]/\sqrt{2}$ notation that we use. Instead, there is an extra negative sign: $Y_1^{\pm 1}(\theta,\phi) = \mp F(\theta)e^{\pm i\phi} = \mp F(\theta)[\cos(\phi) \pm i\sin(\phi)] \sim \mp[|e_x\rangle \pm i|e_y\rangle]$ on which basis the angular momentum ladder operators are defined as $\hat{l}_{\pm}|Y_1^0\rangle = \sqrt{2}|Y_1^{\pm}\rangle$.
[75] G. Thiering and A. Gali, "Nuclear spin relaxation in solid state defect quantum bits via electron-phonon coupling in their optical excited state," (2024), arXiv:2402.19418 [quant-ph].
[76] M. Mohseni, L. Razinkovas, V. Žalandauskas, G. Thiering, and A. Gali, "Magneto-optical properties of group-iv–vacancy centers in diamond upon hydrostatic pressure," (2024), arXiv-toDO:xxxx.xxxx [quant-ph].
[77] M. Gajdoš, K. Hummer, G. Kresse, J. Furthmüller, and F. Bechstedt, Phys. Rev. B **73**, 045112 (2006).
[78] V. Weisskopf and E. Wigner, Z. Physik **63**, 54 (1930).
[79] M. L. Goldman, M. W. Doherty, A. Sipahigil, N. Y. Yao, S. D. Bennett, N. B. Manson, A. Kubanek, and M. D. Lukin, Physical Review B **91**, 165201 (2015).
[80] D. Braukmann, E. R. Glaser, T. A. Kennedy, M. Bayer, and J. Debus, Physical Review B **97** (2018), 10.1103/physrevb.97.195448.

[81] M. Goldman, A. Sipahigil, M. Doherty, N. Yao, S. Bennett, M. Markham, D. Twitchen, N. Manson, A. Kubanek, and M. Lukin, Physical Review Letters **114**, 145502 (2015).

[82] G. Thiering and A. Gali, Physical Review B **98** (2018), 10.1103/physrevb.98.085207.

[83] C. M. Marian, Wiley Interdisciplinary Reviews: Computational Molecular Science **2**, 187 (2011).

[84] K. D. Jahnke, A. Sipahigil, J. M. Binder, M. W. Doherty, M. Metsch, L. J. Rogers, N. B. Manson, M. D. Lukin, and F. Jelezko, New Journal of Physics **17**, 043011 (2015).

[85] Extrapolating γ_- in Eq. (5) that of Ref. 84 at $T = 0$ K and $\Delta = 47$ meV leads to orbital relaxation time in the fs regime.

[86] M. Bockstedte, F. Schütz, T. Garratt, V. Ivády, and A. Gali, npj Quantum Materials **3** (2018), 10.1038/s41535-018-0103-6.

[87] E. Londero, E. Bourgeois, M. Nesladek, and A. Gali, Phys. Rev. B **97**, 241202(R) (2018).

[88] P. Siyushev, H. Pinto, M. Vörös, A. Gali, F. Jelezko, and J. Wrachtrup, Physical Review Letters **110** (2013), 10.1103/physrevlett.110.167402.

[89] D. Wirtitsch, G. Wachter, S. Reisenbauer, M. Gulka, V. Ivády, F. Jelezko, A. Gali, M. Nesladek, and M. Trupke, Phys. Rev. Res. **5**, 013014 (2023).

[90] N. Aslam, G. Waldherr, P. Neumann, F. Jelezko, and J. Wrachtrup, New Journal of Physics **15**, 013064 (2013).

[91] R. Ulbricht and Z.-H. Loh, Physical Review B **98** (2018), 10.1103/physrevb.98.094309.

[92] L. Hacquebard and L. Childress, Phys. Rev. A **97**, 063408 (2018).